*Annu. Rev. Nucl. Part. Sci. 1994. 14:453–500*


# CRYSTAL CALORIMETERS IN PARTICLE PHYSICS

*G. Gratta, H. Newman, and R. Y. Zhu*

California Institute of Technology, Pasadena, California 91125

KEY WORDS: experiment, high-energy physics, particle physics, experimental physics, detector



CONTENTS



## 1. INTRODUCTION

Total absorption shower counters made of inorganic scintillating crystals have been known for decades for their superb energy resolution and detection efficiency. In high-energy physics, large arrays of scintillating crystals have been assembled for precise measurement of the energy and angle of photons and electrons. The Crystal Ball detector (1) first demonstrated the discovery potential of crystal calorimeters through its study of radiative transitions and decays of charmonium states (Fig-



0163-8998/94/1201-0453$05.00

ure 1) (2). Over the past decade, following the Crystal Ball and CUSB (3) experiments, larger crystal calorimeters have been constructed, and their use has been a key factor in the successful physics programs of the L3 experiment at LEP (4), of CLEO II at CESR (5), and of the Crystal Barrel at LEAR (6). Similar crystal detector arrays have been designed and are under development for the next generation of high-energy physics experiments aimed at the study of CP violations. These arrays include KTeV at Fermilab (7) and the SLAC (8) and KEK (9) B Factory detectors.

In addition, a large sector of the high-energy physics community has designed and studied crystal calorimeters containing $10^4$ to more than $10^5$ elements, planning to use them in experiments for multi-TeV hadron colliders, including the late Superconducting SuperCollider (SSC) in

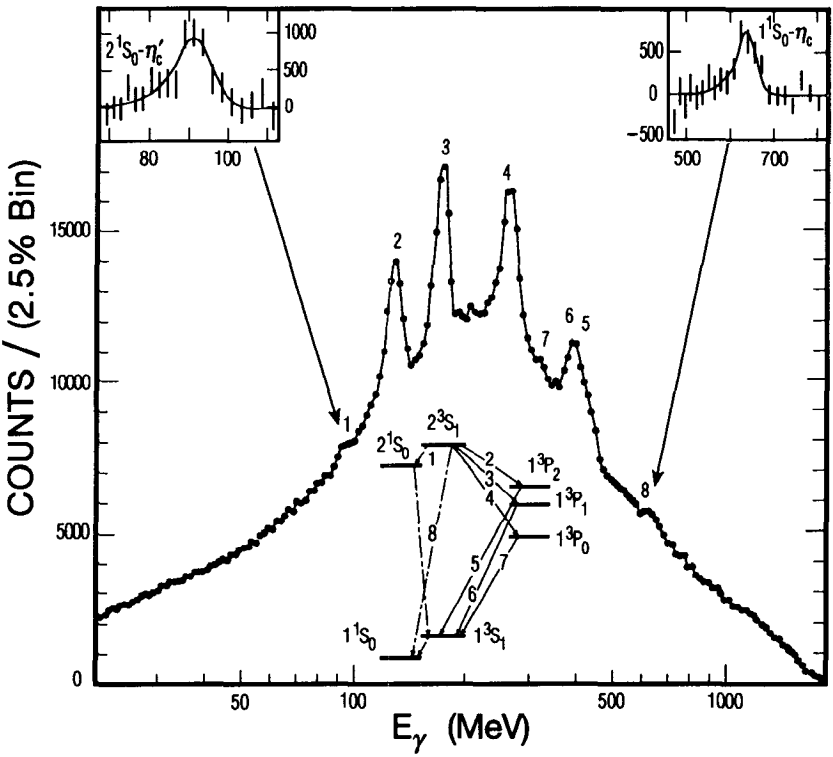


*Figure 1* An inclusive photon spectrum measured at the $\psi(3686)$ resonance by the Crystal Ball experiment at SLAC. Almost all of the principal radiative transitions of the charmonium system are observed simultaneously (2). The upper inserts show the background subtracted signal from $\eta_c(2980)$ and $\eta_c(3590)$ states.

the US (10, 11) and the Large Hadronic Collider (LHC) at CERN in Europe (12, 13). Although some of these crystal detector designs (10, 11, 13) are no longer under consideration for use in an experiment, their development led to significant advances in our understanding of the physics capabilities of these detectors and key advances in crystal-detector technology. We therefore include these designs in this review. At the time of this writing, a crystal calorimeter is being considered as an option for the CMS electromagnetic calorimeter at the LHC.

The unique physics capability of a crystal calorimeter results from its high electron and photon energy resolution over a wide energy range, uniform hermetic coverage, fine granularity over a large solid angle, and clean electron and photon identification. The combined energy and position resolution of these detector systems results in the best efficiency (and signal-to-background ratio) for the reconstruction of multilepton, lepton-photon, and multiphoton invariant masses as well as in a clean separation of electrons from jets and single hadrons. A well-designed crystal calorimeter has greater sensitivity than sampling calorimeters (in which the detection medium is interleaved with, or embedded in, a matrix of inert material) for detecting multibody final states containing low-mass resonances (such as $\pi^0$, $\eta$, and $\eta'$), or yet-to-be-discovered high-mass particles such as the Higgs in the intermediate mass range between 80 and 170 GeV. Experiments that include large crystal calorimeters thus have the capability of isolating rare new physics events from standard physics backgrounds. Figure 1 shows an example for the Crystal Ball NaI(Tl) calorimeter.

To maintain the high resolution and the resultant sensitivity to new physics in situ, the detector must be resistant to radiation damage and allow for precision calibration in addition to high speed, mechanical robustness, and a stable readout with high linearity and large dynamic range. For experiments that must operate in the high-rate, high-radiation environment of multi-TeV hadron colliders, very high speed (triggering within the typical beam-crossing time of 25 ns) and radiation resistance up the 10 Mrad range are among the principal design requirements. These needs have led to the choice of $BaF_2$, $CeF_3$, pure CsI, or other new high-density fluorides as the candidate crystals. At lower energies, high-luminosity experiments designed to search for rare B, K, or $\tau$ decays, or to perform precise CP violation measurements through the study of B and K decays to states containing $e^+e^-$ pairs or single or multiphotons (including $\pi^0$ and decays) have chosen CsI(Tl) (CLEO II, Crystal Barrel, SLAC, and KEK B Factories) or undoped CsI (KTeV). This choice offers a mechanically robust solution to the requirements of high light output, a minimum of material in front of and

between the crystals, radiation hardness up to 10 krad, and moderate to high signal speed.

## 2. INORGANIC CRYSTAL SCINTILLATORS

Table 1 (based on Refs. 14–18) lists the basic properties of commonly used heavy crystal scintillators: NaI(Tl), CsI(Tl), undoped CsI, $BaF_2$, $CeF_3$, and BGO ($Bi_4Ge_3O_{12}$). Except for $CeF_3$, these crystals are commercially available in large quantities. The expected price/cm$^3$ listed in the table corresponds to typical quotations for an order of large crystals totaling $10^6$ cm$^3$ and in some cases more than $10^7$ cm$^3$.

The choice of crystal for a calorimeter is governed by the characteristics and related considerations summarized below:

MATERIAL PROPERTIES Density, melting point, speed of growth, breaking stress, machinability (cleaving), quality of crystal structure, flatness and crystal structure of polished surfaces, and hygroscopicity all affect the production rate, net yield, and price. They also determine the minimum thickness of support material that must be placed in front of and between the crystals, which may affect the energy resolution.

**Table 1** Properties of some heavy scintillators

| | NaI (Tl) | CsI (Tl) | Pure CsI | $BaF_2$ | $CeF_3$ | BGO |
|---|---|---|---|---|---|---|
| Density (g cm$^{-3}$) | 3.67 | 4.51 | 4.51 | 4.89 | 6.16 | 7.13 |
| Melting point (°C) | 651 | 621 | 621 | 1280 | 1460 | 1050 |
| Radiation length (cm) | 2.59 | 1.85 | 1.85 | 2.06 | 1.68 | 1.12 |
| Molière radius (cm) | 4.8 | 3.5 | 3.5 | 3.39 | 2.63 | 2.33 |
| Interaction length (cm) | 41.4 | 37.0 | 37.0 | 29.9 | 26.2 | 21.8 |
| Refractive index[a] | 1.85 | 1.79 | 1.95 | 1.50 | 1.62 | 2.15 |
| Hygroscopic | Yes | Slightly | Slightly | No | No | No |
| Luminescence (nm)[b] | 410 | 550 | 565 | 310 | 340 | 480 |
| Peak wavelength | | | 315 | 220 | 300 | |
| Decay time (ns) | 230 | 1000 | 35 | 630 | 30 | 300 |
| | | | 6 | 0.9 | 9 | |
| Relative light output[c] | 100 | 45 | 4 | 20 | 3.5 | 13 |
| | | | 2 | 4 | 3.5 | |
| Price ($/cm$^3$) | 1–2 | 2 | 3 | 2.5 | 3[d] | 7 |

[a] At the wavelength of the emission maximum.
[b] For luminescence, decay time, and relative light output, the top line gives the slow scintillation component, and the bottom line gives the fast scintillation component.
[c] Measured with a PMT with a bialkali cathode.
[d] Expected price for mass-production.

SHOWER CONTAINMENT Radiation length ($X_0$) and Molière radius ($R_M$) are the important factors here. Dense crystals with a shorter $X_0$ offer a smaller crystal length for longitudinal containment of high-energy electromagnetic showers. For most applications up to the TeV range, 23–25 $X_0$ is sufficient. Above 100 GeV, tail suppression to high accuracy (as in KTeV) requires 27 $X_0$ or more. Lateral containment is controlled by $R_M$. Of the energy deposited near the longitudinal position of the shower peak, 93% is contained within a perpendicular distance of $\approx 1.5\ R_M$ from the direction of an incident photon.

SCINTILLATION PROPERTIES These include light frequency, decay speed, and temperature dependence. Scintillators in the far UV (such as $BaF_2$ fast component) must be read out by photosensors with special photocathodes and/or windows. Long light attenuation lengths sufficient for uniform response along the crystal (often limited by the efficiency for reflection at the surfaces) are more difficult to achieve for wavelengths below 300 nm. High speed is an advantage for operation at multi-TeV hadron colliders, particularly for triggering the detector in less than 25 ns between beam crossings. However, the readout must be able to match this speed, leading to a preference for low capacitance (~10 pf) vacuum photodevices (which can operate in moderate magnetic fields). Stability of response, and calibrations precise to <0.5%, are easier to achieve if the light output is temperature independent (as in the case of the $BaF_2$ fast component).

RADIATION RESISTANCE Stability of response up to doses of ~10 Mrad at multi-TeV hadron colliders and ~10 krad at B factories are required for a stable response, and hence for a high resolution.

As summarized below, $BaF_2$, $CeF_3$, and pure CsI are particularly well suited for experiments at future multi-TeV hadron colliders. The commonly used crystals and their main characteristics are as follows:

- NaI(Tl): high light yield; emission well matched to bialkali photocathodes; highly hygroscopic and thus difficult to handle.
- CsI(Tl): high light yield; emission well matched to solid-state photodiodes; high plasticity and resistance to cracking (mechanically robust); slightly hygroscopic. Careful surface treatment is needed; radiation hardness is still under study (17, 19).
- Pure CsI: relatively fast; emission matched to bialkali cathodes. Otherwise the similar to CsI(Tl) (but may be more difficult to grow).
- $BaF_2$: the fast component is the fastest scintillation signal and is temperature independent (20); intrinsically radiation hard up to the

Mrad range (21), but commercially available samples display variable radiation hardness (14, 22); radiation damage is annealable with visible light (23).

- $CeF_3$: relatively new scintillator (24); relatively fast; light yield nearly temperature independent (18); emission matched to bialkali cathodes; smaller $X_0$ and $R_M$ than $BaF_2$; radiation hardness is under study (18, 25).
- BGO: very high density and short $X_0$, $R_M$; emission well matched to photodiodes; not hygroscopic and easy to handle; radiation damage (up to the krad range) (26, 27) can be reduced by Eu doping (28).

In addition to the crystals listed in Table 1, three other heavy crystals were recently studied: $PbWO_4$ (lead tungstate) (29), $PbF_2$ (30), and Ce-doped lutetium oxyorthosilicate [$Lu_2(SiO_4)O$, or LSO, i.e. $Lu_{2(1-x)}Ce_{2x}(SiO_4)O$ (31)].

$PbWO_4$ is a very dense (8.28 g $cm^{-3}$) material with the shortest radiation length (0.85 cm) and Molière radius (2.2 cm). Its scintillation light is peaked at 440 and 530 nm (29), with decay times of 10 and 40 ns. The main shortcomings of this material are the low light yield (10–15 photoelectrons/MeV measured with a bialkali photocathode) and the strong temperature dependence of the scintillation light ($-1.9\%/°C$), in addition to the radiation damage observed (29, 32). The CMS collaboration at CERN is currently studying $PbWO_4$ as an alternative to $CeF_3$ for a crystal electromagnetic calorimeter.

$PbF_2$ is another material of high density (7.77 g/$cm^3$, $X_0 = 0.93$ cm, $R_M = 2.21$ cm) but it is not a scintillator in its most common form. Attempts to dope $PbF_2$ or to grow a crystal with a different structure (33) that scintillates have not been successful. Therefore, it does not really belong in this section—it is a Cherenkov radiator—but we mention it because substantial efforts have been devoted to convert it into a low-cost scintillator.

LSO is also dense (7.41 g $cm^{-3}$, $X_0 = 1.14$ cm, $R_M = 2.3$ cm; similar to BGO). Its scintillation light peaks at 440 nm (a good match to bialkali cathodes), has a decay time of 40 ns, and its light output is 75% of NaI(Tl). Tests have also shown that it is radiation resistant to 100 Mrad (34). The main obstacles to large-scale use of LSO are its very high melting point (>2000°C) and very high price (~\$100/$cm^3$ for crystals produced during research and development). Ce-doped GSO [$Gd_2(SiO_4)O$ (35)] has similar desirable properties and practical drawbacks.

# 3. CRYSTAL CALORIMETERS

Tables 2 and 3 list the main parameters of major crystal calorimeter projects of the recent past (Crystal Ball), present (L3, CLEO II, Crystal Barrel), and future (KTeV, B factories, CMS). The $BaF_2$ calorimeter design for the GEM experiment (11) at the SSC and the $CeF_3$ calorimeter design for the L3P experiment at the LHC (13) are included for completeness. The parameters $\mathbf{a}_0$ and $\mathbf{a}_1$ listed in Tables 2 and 3 represent the contributions to the energy resolution (at 1 GeV) from photoelectron statistics and noise, respectively, as discussed in Section 4.1. Figure 2 shows the crystal arrangement of the L3 BGO calorimeter as an example.

The details of the design of each crystal calorimeter are governed by its physics goals, which usually demand precision measurements of photons and electrons. Examples include: detection and study of radiative transitions of the $J/\Psi$ and $\Upsilon$ resonances (Crystal Ball); measurements of new states decaying to leptons and photons and precision electroweak tests (L3); searches for new resonances decaying to multiple $\pi^0$, $\eta$, and $\omega$ (L3, Crystal Barrel); studies of $\Upsilon$ transitions, $\tau$ branchings to multi-$\pi^0$ and $\eta$ final states, and rare B and $\tau$ decays (CLEO);

**Table 2** Crystal calorimeter parameters

| Experiment<br>accelerator | C. Ball<br>SPEAR | L3<br>LEP | CLEO II<br>CESR | C. Barrel<br>LEAR | KTeV<br>Tevatron |
|---|---|---|---|---|---|
| Inner radius (m) | 0.254 | 0.55 | 1.0 | 0.27 | — |
| B field (Tesla) | — | 0.5 | 1.5 | 1.5 | — |
| Number of crystals | 672 | 11,400 | 7800 | 1400 | 3300 |
| Crystal type | NaI (Tl) | BGO | CsI (Tl) | CsI (Tl) | CsI |
| Crystal length ($X_0$) | 16 | 22 | 16 | 16 | 27 |
| Light output (p.e./MeV) | 350 | 1400 | 5000 | 2000 | 40 |
| Photosensor | PMT[a] | Si PD[b] | Si PD | WS[c] + Si PD | PMT |
| Gain of photosensor | Large | 1 | 1 | 1 | 4000 |
| Noise/channel (MeV) | 0.05 | 0.8 | 0.5 | 0.2 | Small |
| Dynamic range | $10^4$ | $10^5$ | $10^4$ | $10^4$ | $10^4$ |
| $a_0$[d] (%) | <0.1 | 0.3 | 0.2 | <0.1 | <0.1 |
| $a_1$[e] (%) | 0.2 | 0.1 | 0.05 | 0.07 | 0.5 |

[a] Photomultiplier tube.
[b] Silicon photodiode.
[c] Wavelength shifter.
[d] Noise contribution to the energy resolution (at 1 GeV).
[e] Photoelectron statistics contribution to the energy resolution (at 1 GeV).

**Table 3** Parameters of recently designed crystal calorimeters

| | BaBar SLAC | KEK BF KEK | CMS LHC | (GEM) SSC | (L3P) LHC |
|---|---|---|---|---|---|
| Inner radius (m) | 1.0 | 1.25 | 1.3 | 0.8 | 2.9 |
| Segmentation $\Delta\eta$ | — | — | 0.02 | 0.04 | 0.01 |
| B field (Tesla) | 1.0 | 1.0 | 4.0 | 0.8 | 2.0 |
| Number of crystals | 10,000 | 8900 | 43,200 | 15,000 | 129,600 |
| Crystal type | CsI (Tl) | CsI (Tl) | $CeF_3$ | $BaF_2$ | $CeF_3$ |
| Crystal length ($X_0$) | 18 | 16 | 25 | 24.5 | 23.2 |
| Light output (p.e./MeV) | 5000 | 5000 | 300 | 30 | 50 |
| Photosensor | Si PD | Si PD | Si PD | VPT | VPT |
| Gain of photosensor | 1 | 1 | 1 | 12 | 10 |
| Noise/channel (MeV) | 0.1 | 0.1 | 20 | 3 | 20 |
| Dynamic range | $10^4$ | $10^4$ | $10^5$ | $10^5$ | $10^5$ |
| $a_0$[a] (%) | <0.1 | <0.1 | 6 | 1 | 6 |
| $a_1$[b] (%) | 0.03 | 0.03 | 0.2 | 0.6 | 0.5 |

[a] Noise contribution to the energy resolution (at 1 GeV).
[b] Photoelectron statistics contribution to the energy resolution (at 1 GeV).

analyses of $K^0$ mesons and rare decays and precise measurements of CP violation (KTeV); measurements of B mesons and rare decays and test of CP violation (SLAC and KEK B factories); and the origin of electroweak symmetry breaking and Higgs boson detection (CMS, GEM, L3P). The crystal choice, crystal length, and segmentation are adapted to these physics goals, specifically the optimization of mass resolution and/or background rejection.

At low energies (below a few hundred MeV), large light yields (photoelectrons/MeV) are needed to achieve good energy resolution. These requirements have been met by the Crystal Ball using NaI, by CLEO II, and the Crystal Barrel, and in the future by the B factory detectors using Tl-doped CsI, and to a lesser extent by L3 using BGO. Figure 3 (36) shows the $\chi_b$ signal in the inclusive photon spectrum of the decay $\Upsilon(3S) \rightarrow \gamma\chi_b(2P)$, obtained by CLEO II. Because CLEO II uses silicon photodiodes (Si PD), the main contribution to the energy resolution for particles with energies below 200 MeV is electronic noise. Minimization of the inactive material in the front of calorimeter and between the crystals is also required to maintain good resolution at low energies.

At high energies (above a few tens GeV), the energy resolution of a crystal calorimeter is dominated by systematic nonuniformities and variations. To achieve a systematic accuracy of <0.5%, the crystals must be long enough to reduce the rear leakage to the few percent level,

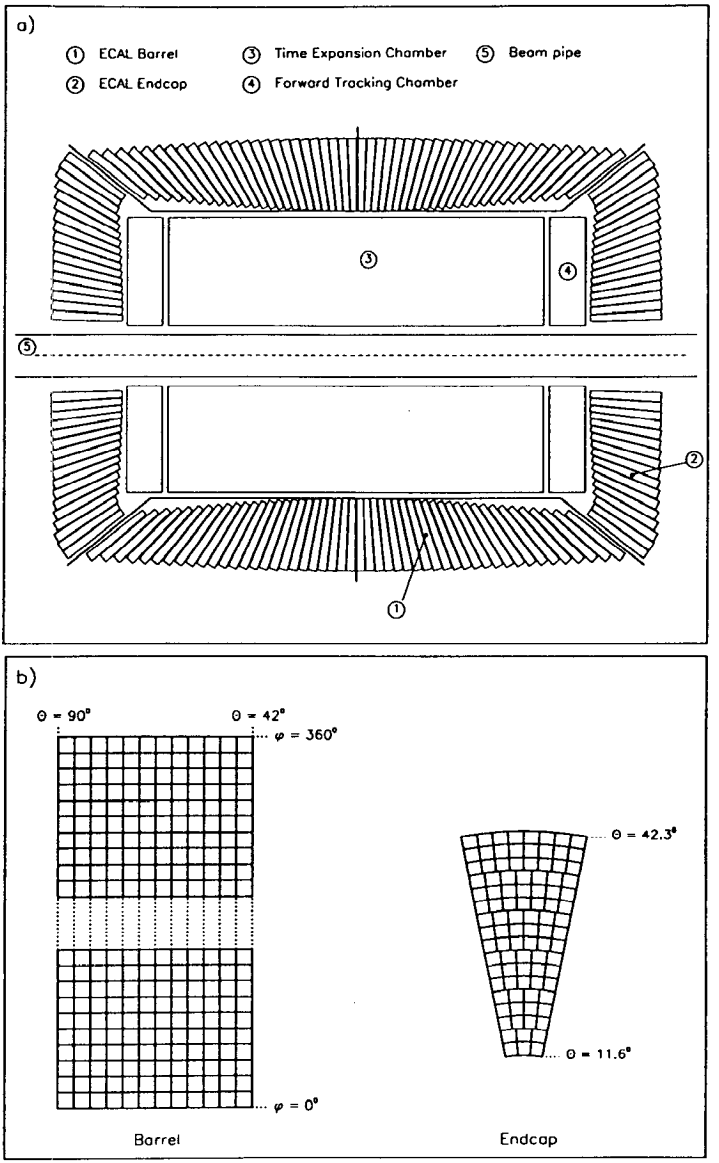


*Figure 2* The L3 BGO calorimeter. *(a)* A longitudinal cut through the detector. *(b)* Details of the crystal arrangement in the barrel and one endcap.

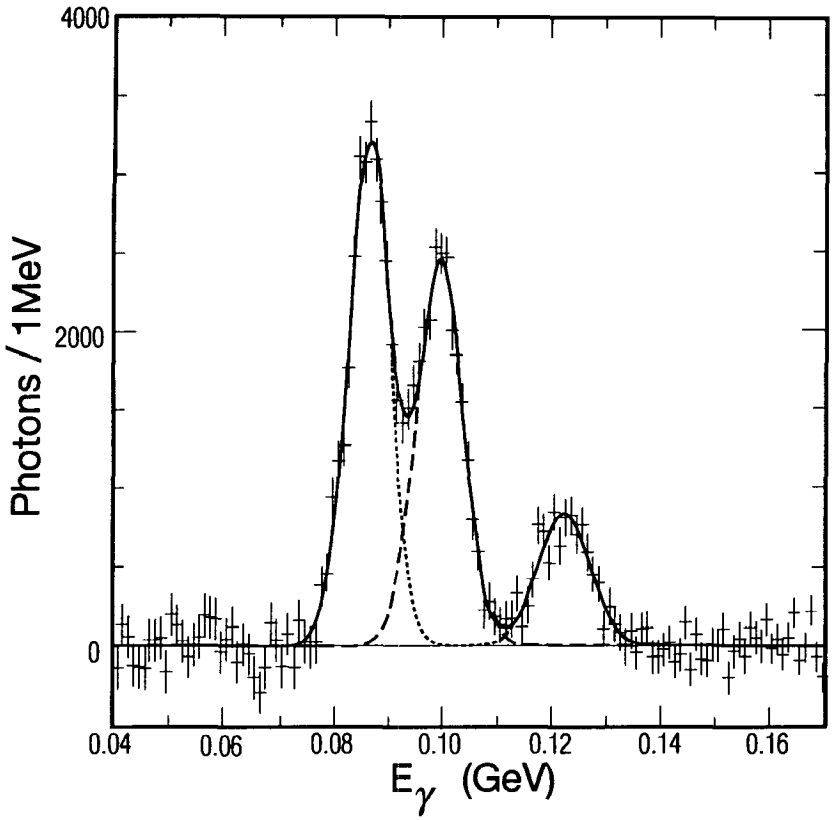


*Figure 3* Inclusive photons in hadronic events measured by CLEO II showing the three photon lines from the radiative decay of $\Upsilon$ (3S) to the three $\chi_b$ (2P) states (36).

and they must be radiation resistant so that uniform light response can be maintained to ~5% over the length of the crystal. The intrinsic mass resolution (without radiative tail) for a 90-GeV photon pair or an $e^+e^-$ pair achieved by L3 is <1% and is expected to be in the 0.5% range once improved calibration techniques are implemented (see Section 7). The CMS, L3P, and GEM projects have aimed at a mass resolution of ~0.4% for a photon pair from $H^0 \rightarrow \gamma\gamma$. In the case of KTeV, the crystal depth (27 $X_0$) is also dictated by the requirement that the tail of the energy resolution function be small enough that an absolute systematic uncertainty of 0.02% in the $\gamma$-energy scale can be attained following extensive calibration (7).

The choice of the inner radius of a crystal calorimeter represents a trade-off between the required performance and cost. A larger radius

would provide better $2\gamma$ separation, and thus higher efficiency of $\pi^0$ reconstruction and/or rejection, at the expense of a larger volume of crystals. The choice of the lateral segmentation represents a trade-off between position resolution (see Section 4.2), which improves with finer segmentation, and the number of readout channels. Longitudinal segmentation of the crystals would provide an angular measurement for high-energy isolated photons (see Section 4.3). This measurement would be advantageous at future hadron colliders for the determination of the vertex of the photon pair at luminosities in the $10^{34}$ $cm^{-2}$ $s^{-1}$ range, where multiple minimum-bias events will overlap with the event of interest at every bunch crossing. However, longitudinal segmentation would require a much greater number of crystal pieces and readout channels.

The choice of the photosensor and its gain are governed by the magnetic field, the crystal type (e.g. by the wavelength of the scintillation light), and the energy-equivalent noise per channel. Operation in a magnetic field excludes the possibility of using most multistage vacuum phototubes. The photosensor choices include solid-state photodiodes, vacuum diodes, or triodes (VPT) (37), or proximity-focused, few-stage, mesh tubes recently developed by Hammamatsu K. K. in Japan (38). For multi-TeV hadron colliders, the sensor must also be radiation hard. Finally, the dynamic range and precision of the readout must cover both the high-energy electrons or photons of interest to extract the physics signals and the particles of much lower energy used for calibrations.



## 4. CRYSTAL CALORIMETER PERFORMANCE

### 4.1 *Energy Resolution*

The energy resolution of an electromagnetic calorimeter can be parametrized as

$$\left(\frac{\Delta E}{E}\right)^2 = \left(\frac{\mathbf{a}_0}{E}\right)^2 + \left(\frac{\mathbf{a}_1}{\sqrt{E}}\right)^2 + \mathbf{b}^2, \qquad 1.$$

where $\mathbf{a}_0$ is the contribution from electronic noise, summed over the readout channels within a few Molière radii around the center of the lateral shower distribution, and $\mathbf{a}_1$ is the contribution from the photoelectron statistics, related to the photon yield in the crystal and the fraction of the end face of the crystal that is covered by the photosensor. The systematic, or constant, term $\mathbf{b}$ has three main contributions:

$$\mathbf{b}^2 = \mathbf{b}_G^2 + \mathbf{b}_C^2 + \mathbf{b}_n^2. \qquad 2.$$

Here, $\mathbf{b}_G$ represents the geometry effect, including shower leakage from the back, side, and front (albedo), and the absorption of part of the shower in the inactive material in front of and between the crystals. The typical lower limit of $\mathbf{b}_G$ is 0.3–0.4%, and it may become larger at both the lower and upper ends of the energy range of interest. The term $\mathbf{b}_C$ represents the intercalibration error of the crystals. Depending on the calibration method(s), the typical lower limit on this term is 0.3%. The term $\mathbf{b}_n$ is the contribution from nonuniformities in the crystal response (resulting from intrinsic attenuation length, variations of the reflectivity as a function of position, or radiation-induced nonuniformities). This term contributes to the resolution because the depth and widths of an electromagnetic shower fluctuate for particles of the same incident energy.

The overlap of particles from different beam interactions within the gating time of the detector also contributes to the energy resolution. This contribution, known as pileup noise, is a significant problem for calorimeters operating at a very high-luminosity ($10^{34}\,cm^{-2}\,s^{-1}$) hadron colliders such as LHC. A detailed discussion of pileup noise is available (12, 13). One way to reduce the pileup noise contribution is to enhance the segmentation by placing the crystal calorimeter at a large distance from the beam line, at the expense of a large calorimeter volume (13).

Compared with the effects mentioned above, the intrinsic resolution resulting from fluctuations in shower development (for a perfectly uniform very large single crystal) is negligible in the energy range of interest for high-energy physics experiments.

4.1.1 NOISE AND SAMPLING TERMS At low energy $E$ the dominant contributions to the energy resolution are *(a)* the electronic noise term ($\mathbf{a}_0/\mathbf{E}$) and *(b)* the pileup noise in the case of very high luminosity, both of which decrease quickly with increasing energy. The sampling term ($\mathbf{a}_1/\sqrt{\mathbf{E}}$) dominates for medium to high energies, up to the high-energy limit at which the systematic term (**b**) becomes dominant. Tables 2 and 3 list the values of the coefficients $\mathbf{a}_0$ and $\mathbf{a}_1$ for various crystal calorimeter systems. Each table entry is calculated analytically using the energy-equivalent noise (in MeV) per readout channel and the light output per unit energy deposited (photoelectrons/MeV), and assuming a summation over an array of $3 \times 3$ crystals for the detection of a shower generated by an electron or photon.

The energy-equivalent electronic noise also determines the lower limit of the energy reach of a crystal calorimeter as well as the resolution and photon identification efficiency at low energies. For a given type

of crystal, the choice of photosensor determines this term. In the case of a solid-state photodiode, the noise is controlled by the diode's area and thickness and by the fraction of the rear crystal face covered. A larger collection area corresponds to a larger signal per unit energy but also to a larger electronic noise, caused by the larger capacitance and leakage current.

The thickness of a diode also determines the (relatively large) energy loss of a particle passing through the diode. This energy may have a significant effect on the resolution at very high luminosity or for crystals that are not deep enough to fully contain the electromagnetic shower.

4.1.2 CONSTANT TERMS The resolution at high energies is limited by systematics. The requirements and means of controlling the terms $\mathbf{b}_n$ and $\mathbf{b}_C$ are discussed later in this section and in Section 7, respectively. Once a sufficiently precise intercalibration and uniform light response are achieved, however, the ultimate energy resolution of a crystal calorimeter is determined by the shower leakage and absorption term $\mathbf{b}_G$. This term can be reliably estimated by a realistic GEANT (39) simulation, which includes an accurate geometrical representation of the calorimeter support structures, the crystal wrapping material, and the air gaps between crystals. The simulation parameters must be set to allow tracking of the particles down to energies around 0.1 MeV (and to 10 keV for photons in some cases). One can use the same simulation to study $\mathbf{b}_n$ by incorporating nonuniformities in the response to deposited energies as a function of the location in the crystal. This effect is discussed further below.

A typical example that has been studied in detail with a GEANT simulation (14) is a $BaF_2$ matrix consisting of 121 ($11 \times 11$) crystals, as proposed for the L* and GEM experiments. Each crystal is 50 cm long and has the shape of a truncated pyramid with the following dimensions: $3 \times 3$ cm$^2$ in the front, $5 \times 5$ cm$^2$ at the back. The effects included in the simulation are: *(a)* 250 $\mu$m carbon fiber wall between crystals, *(b)* transverse shower leakage because of summation of a limited number of crystals ($3 \times 3$ or $5 \times 5$) in the reconstruction of an electromagnetic cluster, and *(c)* 0.3 radiation lengths of aluminum, representing the beam pipe, the central tracker, and the carbon fiber mechanical support, all located at the front of the $BaF_2$ calorimeter. Particles uniformly enter over the front surface of the central crystal of the array. The energies deposited in each crystal, in the carbon fiber walls between crystals, and in the aluminum as well as those leaking out sideways are recorded. Table 4 lists the result of this simulation for

**Table 4** Projected energy resolution (%) of a $BaF_2$ calorimeter

| $E$ (GeV) | 5 | 10 | 20 | 50 | 100 | 200 | 500 |
|---|---|---|---|---|---|---|---|
| Electrical noise | 0.4 | 0.2 | 0.1 | 0.4 | 0.02 | 0.01 | 0.004 |
| Photoelectron statistics | 0.2 | 0.14 | 0.1 | 0.063 | 0.045 | 0.03 | 0.02 |
| Leakage/absorption ($b_G$) | 0.60 | 0.43 | 0.32 | 0.30 | 0.30 | 0.30 | 0.36 |
| Intercalibration ($b_C$) | 0.40 | 0.40 | 0.40 | 0.40 | 0.40 | 0.40 | 0.40 |
| Total | 0.85 | 0.63 | 0.53 | 0.51 | 0.50 | 0.50 | 0.54 |



electrons with different energies (5, 10, 20, 50, 100, 200, and 500 GeV), in terms of standard deviation $\sigma$ of the peak, defined as the full width at half maximum (FWHM) divided by 2.35. This GEANT simulation predicts a constant term of no less than 0.3%. For very high energies, the systematic contribution is somewhat larger, caused by rear leakage due to limited calorimeter depth.

The light-response uniformity at the level of a few percent over the length of the crystal, except for the first few and the last few radiation lengths, is important to maintain high resolution of a crystal calorimeter. This uniformity is also needed to maintain good linearity over a large dynamic range. The effect of light response uniformity also can be estimated by incorporating a response function into the GEANT simulation. Figure 4 (14) shows the GEANT predictions for the energy fraction (top panel) and the intrinsic energy resolution (bottom panel), calculated by summing the energies deposited in a $3 \times 3$ $BaF_2$ subarray of the crystals, as a function of the uniformity of the light-response. In this simulation, the light response ($Y$) of the crystal is parametrized as a normalized linear function:

$$Y = Y_{25}[1 + \delta(z/25 - 1)], \qquad 3.$$

where $Y_{25}$ represents the light response at the center (25 cm) of a 50-cm long $BaF_2$ crystal, $\delta$ represents the deviation from uniform light response and $z$ is the distance from the small (front) end of a tapered crystal. To maintain a $b_n$ term of $<0.5\%$, the $\delta$ value must be $<5\%$. A detailed study using many different functional forms of the light-response nonuniformity, in addition to a linear dependence, quantitatively confirmed this conclusion (40).

Light-response uniformity can be achieved by using special wrapping or coating techniques. For a tapered crystal with six polished faces, two counterbalancing factors affect the light uniformity over the crystal length: the light attenuation (both bulk attenuation and losses at each reflection) and an optical focusing effect. The optical focusing effect can be understood in terms of Liouville's theorem: as the crystal gets

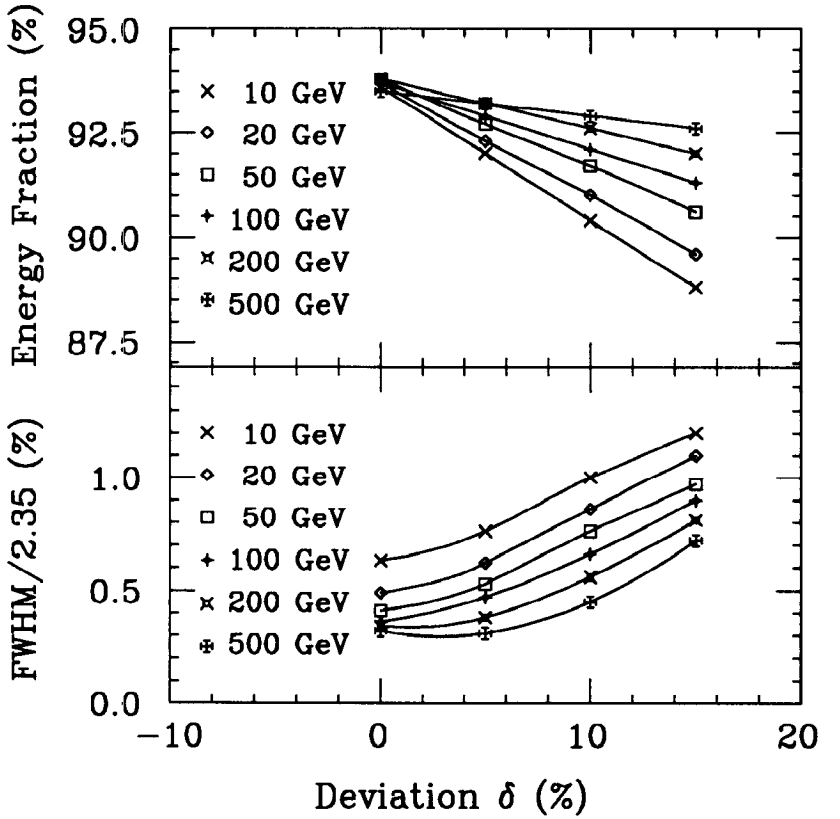


*Figure 4* The relative mean energy fraction and the energy resolution for electromagnetic clusters of 3 × 3 crystals as a function of the nonuniformity of light response, derived with a GEANT Monte Carlo simulation (14). See Equation 3 in the text for the definition of the parameter $\delta$.

larger and a bundle of light rays is allowed to expand, the individual rays within the bundle tend to become more and more parallel to the long axis of the crystal. Although light attenuation causes a decrease of the response with increasing distance from the photosensor, the optical focusing leads to higher light-collection efficiency and thus a greater response with distance. For a 24-cm BGO crystal, the second factor dominates: A strong increase of the light response (up to a factor of 2.4) at the small end compared with the large end was observed for L3 crystals that had all sides well polished (4).

In general, a uniform light response has been obtained by treating part of the crystal surface to avoid the total internal reflection that continues over many bounces and to instead scatter the light diffusely

and randomize the direction of light rays within the crystal. Common techniques are *(a)* depolishing the lateral crystal faces in a nonuniform and carefully controlled manner (Crystal Ball) (41); *(b)* coating all surfaces of the crystals with a highly reflective diffuse reflector, such as a 40–50 $\mu$m coating of NE560 white paint (L3 BGO calorimeter) (4); or *(c)* wrapping with teflon or aluminized mylar (KTeV CsI calorimeter) (7).

Figure 5 shows the light-response uniformity of a 40-cm CsI crystal with teflon wrapping, measured by KTeV (7). A deviation of less than 2.1% over the crystal length is achieved.

In some cases, the required depth of a calorimeter element exceeds the commercially available length for a single crystal. In these cases (e.g. the GEM $BaF_2$ and the CMS $CeF_3$ calorimeters) several pieces of crystals may be glued or otherwise joined to form a unit. Under these circumstances, a glue with good transmission at the wavelength of the scintillation light is essential to make a bond with sufficient light-transmission as well as mechanical strength. Figure 6 shows the transmittance measured for 500-$\mu$m layers of various adhesives. For $BaF_2$, fast scintillation light is in the 200-nm range, and a thin layer (tens of microns) of KE103 glue provides a transmission above 97% (14), as well as high radiation resistance (42).

4.1.3 SUMMARY OF THE ENERGY RESOLUTION Using the $BaF_2$ calorimeter as an example, Table 4 shows all the contributions described in

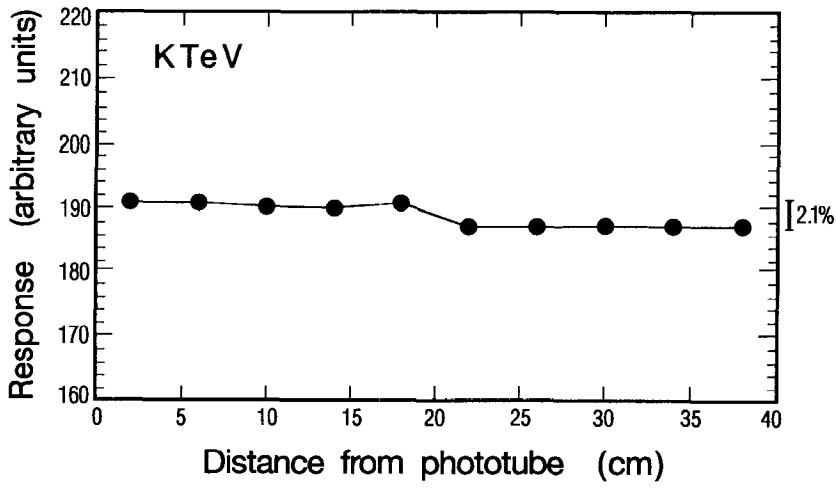


*Figure 5* Light response as a function of the distance from the PMT measured in a 40-cm CsI crystal with teflon wrapping (7). The overall nonuniformity is 2.1%.

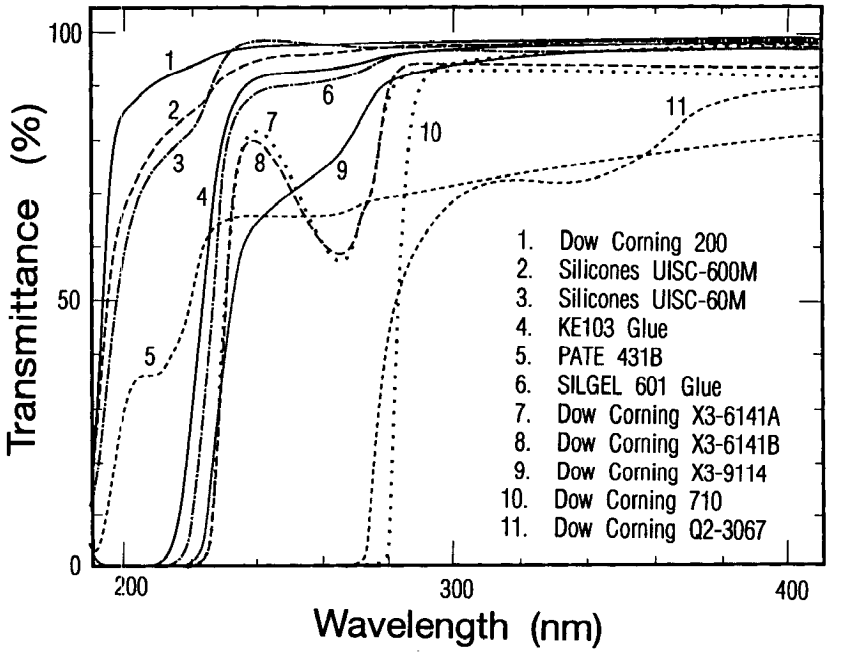


*Figure 6* Transmittance of 500-$\mu$m layers of various grease and glues (14). The typical layer thickness used to couple the photosensors to the crystals in calorimeters is 10–50 $\mu$m.

Section 4.1 and the expected overall energy resolution. An intercalibration accuracy of 0.4% has been assumed (see Section 7 for a discussion). If the nonuniformity ($\mathbf{b_n}$) of the light-response is under control, the dominant contributions to the energy resolution at high-energy are the intercalibration term $\mathbf{b_C}$ and the shower leakage and absorption term $\mathbf{b_G}$. Figure 7*b* shows the resultant energy resolution. For comparison, Figure 7*a* shows the measured energy resolution of 4000 BGO crystals (one half barrel). In the energy range beyond 20 GeV, the dominant contributions to the energy resolution are the systematic terms described above. The data are well reproduced by the simple parameterization of the form $2\%/\sqrt{E} \oplus 0.5\%$.

## 4.2 *Position Resolution*

Accurate position measurement, and hence precise determination of the angles of electrons and photons, is needed if the energy resolution of a crystal calorimeter is to be fully utilized to provide precisely reconstructed invariant masses of resonances decaying to photons or elec-

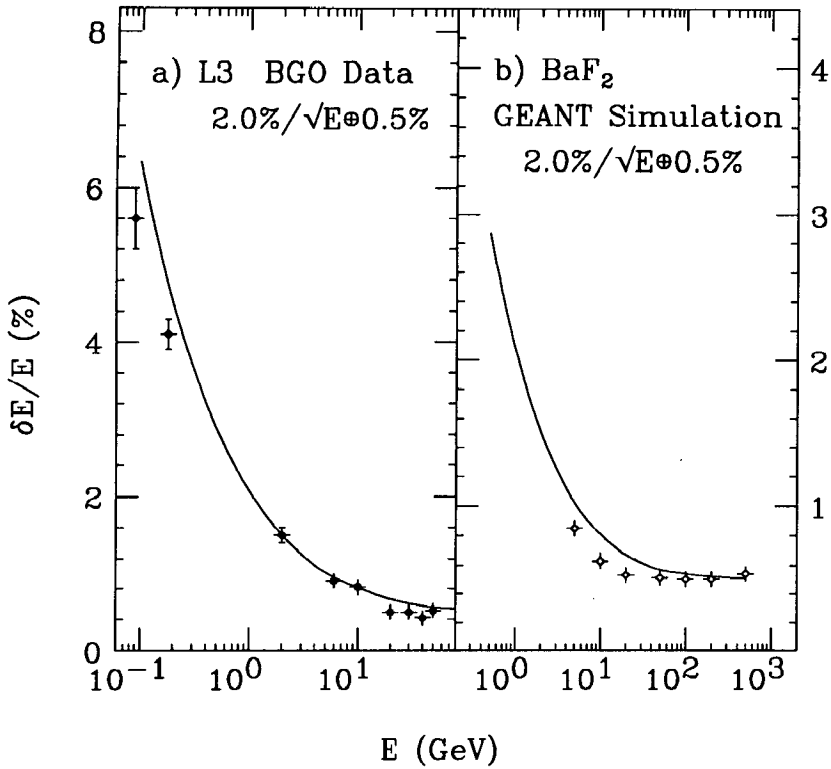


*Figure 7* Energy resolutions of *(a)* a 4000-crystal half-barrel of the L3 BGO calorimeter, measured in test beams at the CERN SPS (2–50 GeV), the LEP injector (180-MeV extracted beam), and CESR (100 MeV) (4) and *(b)* a $BaF_2$ calorimeter, simulated with the parameters listed in Table 4. The solid curves represent the simple parametrization $2\%/\sqrt{E} \oplus 0.5\%$.

trons. This requirement is a key issue in the search for the intermediate-mass Higgs through its rare decay mode $H \rightarrow \gamma\gamma$ (43).

The position of the impact point of an electron or photon on the front face of a calorimeter may be reconstructed from the pattern of energies deposited in a cluster of crystals. The simplest technique is the center-of-gravity method, in which the centroid of an electromagnetic shower is computed from a linear combination of the energies deposited in the crystals:

$$X_{cg} = \sum_i (X_i E_i) \Big/ \sum_i E_i, \qquad 4.$$

where $E_i$ is the energy deposited in the $i$th row along the $x$ direction and $X_i$ is the $x$-coordinate of the center of the $i$th row at the reference plane. The summation can be carried out over the (approximately) square subarray of 25 ($\sum_{25}$), 9 ($\sum_9$), or 5 ($\sum_5$) crystals centered on the crystal with the highest energy deposition. Because of the finite cell size, the measured position $X_{cg}$ is biased toward the center of a cell, such that a uniform flat input distribution in $x$ results in a reconstructed $X_{cg}$ distribution with a characteristic S-shape. One must apply corrections to unfold the S-shape and to obtain an accurately reconstructed position $X_{rec}$.

Because the center-of-gravity method actually calculates the shower center near the shower peak, the above algorithm is accurate only for a calorimeter with a projective geometry and a particle passing through the geometric origin. Otherwise, the algorithm defines an accurate position only for showers of average depth. A shower depth–related correction can be derived from the energy leakage to the hadron calorimeter or from the energy deposited in a longitudinally segmented calorimeter.

Figure 8 (44) shows the relation between $X_{cg}$ and $X_{rec}$, calculated using a GEANT simulation with 5000 $e^+e^-$ events at the $Z$ peak, i.e. $\sqrt{s} = 91.16$ GeV, vs the actual impact point $X_{in}$ for the L3 BGO calorimeter. The correction applied to obtain the reconstructed coordinates was a simple polynomial function. The simulation shows that summation over 9 or 25 crystals provides a reconstruction accuracy with a position resolution of $\leq 0.65$ mm, whereas summation over 5 crystals provides a slightly poorer accuracy of $\leq 0.85$ mm. The simulation agrees very well with the data obtained by L3 at LEP (44). A GEANT simulation for the KTeV CsI calorimeter with 5- and 2.5-cm crystals shows that 1.4- and 0.8-mm position resolution can be achieved for these two block sizes, as shown in Figure 9 (7). The position resolution does not degrade the two-photon invariant mass resolution provided by a crystal calorimeter at multi-TeV hadron colliders, provided that the production point of the photon can be determined by the central tracker (43).

In general, the position resolution of a calorimeter depends on its structure, especially the lateral cell size. The intercalibration among the cells also has an important effect, especially if the calibration is not controlled to the level of 1% or better. The optimum lateral cell dimension is a compromise between good position resolution and the total number of readout channels, which impacts the cost. Good position resolution as well as a good knowledge of the transverse shower shape, which are needed for $e/\pi$ separation and two $\gamma$ separation, favor a small crystal size, whereas shower containment favors a larger size. A cell

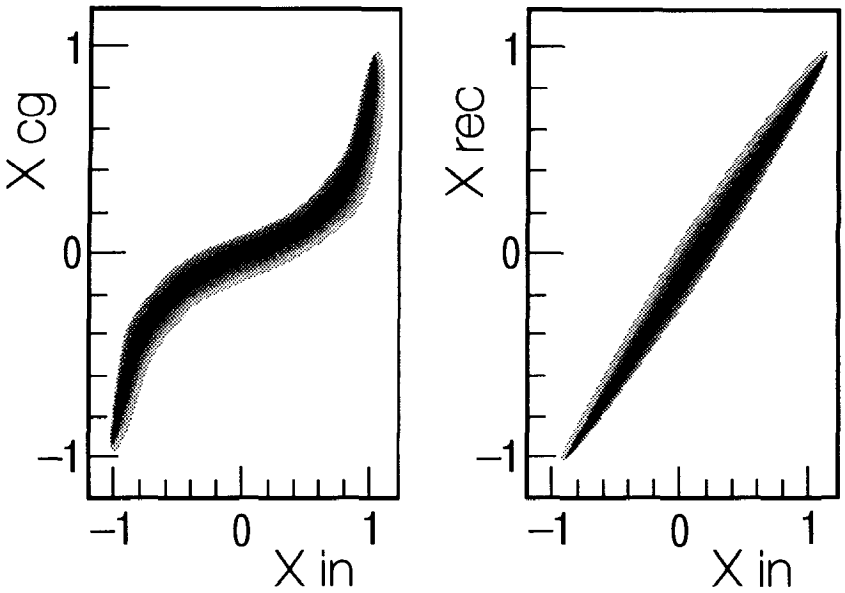


*Figure 8* Correlation between the positions measured with *(a)* the center of gravity method ($X_{cg}$) and *(b)* the reconstructed positions ($X_{rec}$) vs the actual positions ($X_{in}$). The results are derived from 5000 $Z \rightarrow e^+e^-$ decays simulated by the GEANT Monte Carlo in the L3 BGO calorimeter (44).

dimension of approximately one Molière radius ($R_M$) is usually chosen, corresponding to ~75% of the shower energy deposited in the center cell. For example, the front face of an L3 BGO crystal has a dimension of 0.86 $R_M$ × 0.86 $R_M$, whereas the CLEO II CsI(Tl) calorimeter and CMS $CeF_3$ designs have dimensions of 1.4 and 1.0 $R_M$, respectively.

## 4.3 *Angular Resolution*

For some applications, such as the $H \rightarrow \gamma\gamma$ search at multi-TeV hadron colliders (43), it is important to measure the photon direction as well as the energy. The most accurate measurement of the photon direction can be achieved by using the event vertex position determined by the central tracking system and the shower position determined by the center-of-gravity method described in Section 4.2. At very high luminosity, however, the efficiency of Higgs vertex determination would be degraded by the pileup of multiple event vertices in a single bunch crossing. Therefore, an alternative method relies on photon pointing, an angle measurement with the electromagnetic calorimeter itself. This is a necessary feature for crystal calorimeters operated at LHC. (Note that in a collider experiment, the transverse beam dimensions are small

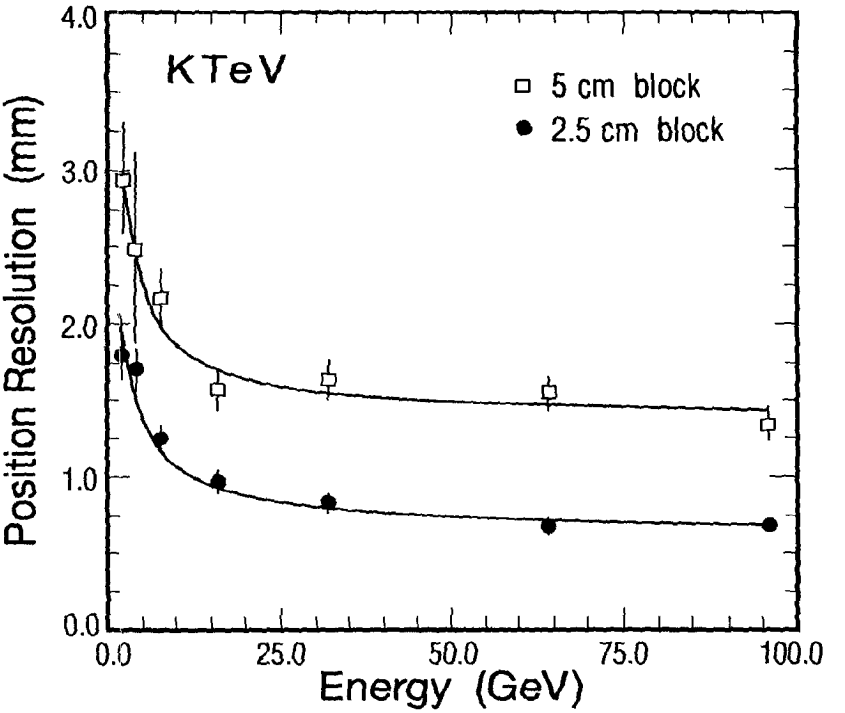


*Figure 9* Position resolution of the KTeV CsI calorimeter, obtained from a GEANT simulation, for 5- and 2.5-cm crystals (7).

and the beam location is accurately known in a plane perpendicular to the direction of the incoming beams. Only the vertex position along the direction of the beams is smeared out by the bunch length. Photon pointing is thus needed to accurately determine the polar angle of electrons or photons with respect to the beam line.)

To measure the photon direction, one must measure the lateral shower position at two depths. Two possible approaches have been suggested and studied: One simply segments the crystal into pieces of 8 $X_0$ in front and 17 $X_0$ at the back; and the other uses a fine-grained position detector at a depth of 4–5 $X_0$ and combines this with a measurement of the shower position in the crystal segments at the back. Although the second approach provides better angular resolution, the first approach allows for a simpler mechanical design. For the first approach, one can further split the front crystal into several pieces to

provide better angular resolution. For example, one of the CMS calorimeter designs has the front segment of each calorimeter cell split into four crystal pieces (12) matched to one much larger piece in the back of the cell. This approach only works with sufficient precision for high-energy photons, such as the >20 GeV photons at future hadron colliders. For low-energy photons, because of the smaller shower length and the fluctuations of the starting point of showers, this approach is not practical.

A simple parametrization of the angular resolution is $\delta\theta(\text{mrad}) = \mathbf{a}/\sqrt{E}$, where $E$ is measured in GeV. GEANT simulations of the CMS $CeF_3$ crystal calorimeter have shown that $\mathbf{a} = 60$ mrad can be achieved by using a front crystal split into four pieces, and $\mathbf{a} = 50$ mrad can be obtained with a precise position detector located at $5X_0$ depth (45) (Figure 10). The angular resolution tends to improve if the position detector is located closer to the front, e.g. at 4 $X_0$ instead of 5 $X_0$ (45).

## 4.4 *Time Resolution*

Time resolution is not important for crystal calorimeters used in a low-rate environment. At $e^+e^-$ colliders, for example, the total cross section is low; at the B-factory luminosity of $10^{33}$ cm$^{-2}$ s$^{-1}$, event rates are below the kHz level. The typical pulse shaping (or gated integration) times for the L3 BGO calorimeter, the CsI(Tl) calorimeter at CLEO II, and the SLAC and KEK B factories are in the range of a few micro-

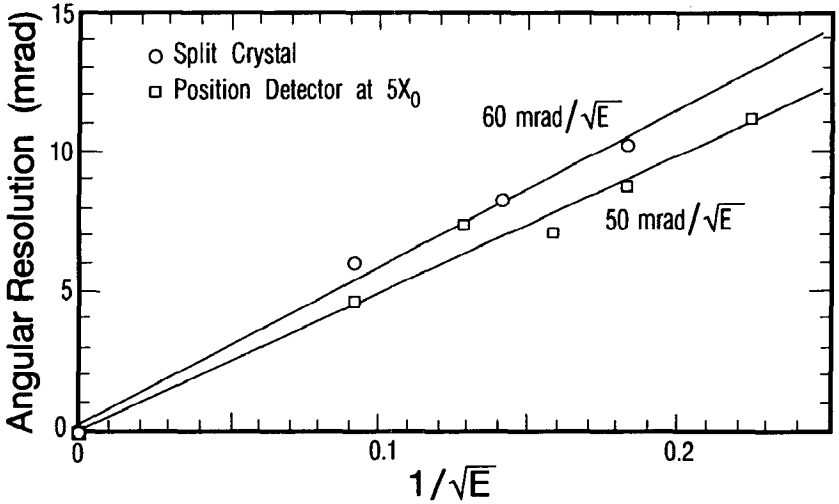


*Figure 10* Angular resolution as a function of photon energy for the CMS $CeF_3$ calorimeter, obtained from GEANT simulations, for two designs with different segmention (45).

seconds. At multi-TeV hadron colliders, because of the 100-mb total cross section, very fast rise times and short decay times are important for triggering as well as for precision energy measurement.

As shown in Table 1, the fastest scintillation response can be obtained from $BaF_2$, which has a fast scintillation component with a decay time of $<1$ ns. However, $BaF_2$ crystals also produce a slow component with a 600-ns decay time and with five times higher intensity. In triggering, the effect of the slow component may be suppressed electronically by sampling the output of each channel twice just before and a few fast decay-times after the start of a pulse (46). However, the intrinsic slow component would limit the dynamic range of the photosensors and lead to pileup noise that degrades the energy resolution. An alternate method of suppressing the slow component is the doping of the $BaF_2$ crystals by lanthanum (47). Doping at an appropriate concentration of lanthanum reduces the slow component by a factor of five, but has no effect on the intensity of the fast components.



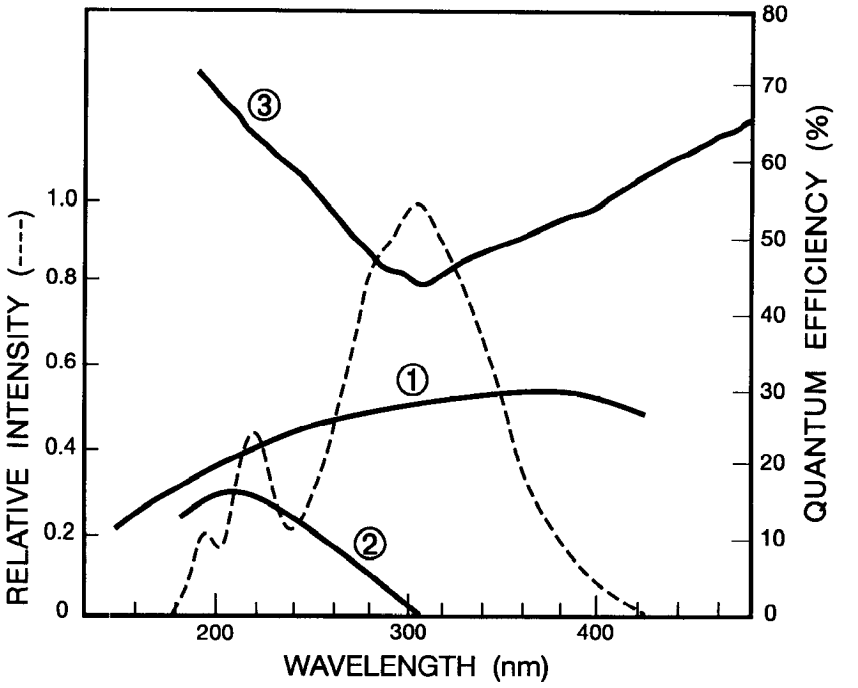


*Figure 11* $BaF_2$ scintillation spectrum *(dashed line)* and quantum efficiencies of (1) a bialkali photocathode, (2) a UV-selective solar-blind Cs-Te photocathode, and (3) a silicon photodiode.

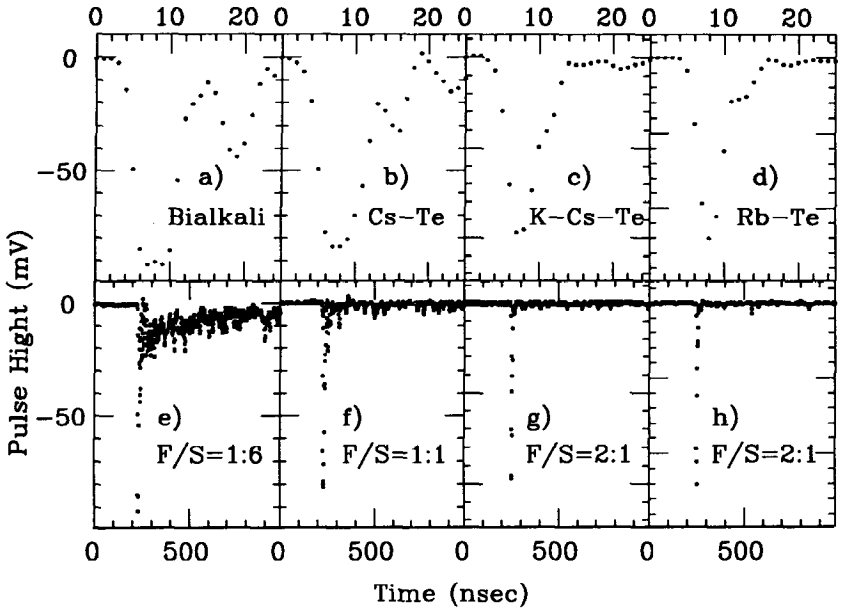


*Figure 12* $BaF_2$ scintillation light pulses observed by a bialkali cathode *(a, e)*, a Cs-Te cathode *(b, f)*, a K-Cs-Te cathode *(c, g)*, and a Rb-Te cathode *(d, h)* (14). The rise time of the scintillation light pulse is dominated entirely by the 2.3-ns rise time of the PMTs. As shown on an expanded scale *(a–d)*, the full width at half maximum of the fast scintillation light is 4–6 ns. The optical suppression factors *(F/S)*, defined as the number of photoelectrons in the fast components *(F)* divided by the number of photoelectrons in the slow component *(S)* are indicated for each cathode.

The fast components in $BaF_2$ also may be selected on the basis of the spectral difference between the two components. The light emission spectrum of the fast component lies mostly below a wavelength of 240 nm, whereas the slow component is mostly above this wavelength. Figure 11 shows the scintillation spectrum (dashed line) of a $BaF_2$ crystal and the quantum efficiencies of *(a)* a bialkali, *(b)* a UV-selective solar-blind Cs-Te photocathode for a vacuum phototube, and *(c)* a silicon photodiode. The solar-blind Cs-Te cathode, which has enhanced sensitivity below 240 nm, is well matched to the fast component of the $BaF_2$ spectrum. Figure 12 shows pictures of the scintillation light pulses recorded by a bialkali photocathode, a Cs-Te photocathode, a K-Cs-Te cathode, and a Rb-Te cathode. The K-Ce-Te and Rb-Te cathodes were developed at Hammamatsu K. K. specifically for $BaF_2$ readout.[1] Researchers there have measured a rise time of 2.3 ns.

[1] The K-Cs-Te cathode has been implemented in the Hammamatsu R4406 triode, and the Rb-Te cathode has been implemented in the R4480 PMT for the $BaF_2$ readout. Both tubes use quartz windows and are commercially available.

Were a silicon photodiode to be used as a readout device, the rise time would be 10–15 ns, as a result of the large capacitance. As shown in Figure 11, however, the silicon photodiode has a sixfold higher quantum efficiency at 220 nm. An interference filter with peak transmittance at 220 nm and a width of 30 nm (as tested at Caltech) could be combined with a silicon photodiode to suppress the slow component while maintaining a better photoelectron yield.



## 5. CRYSTAL RADIATION DAMAGE

All known large crystal scintillators suffer radiation damage.[2] The principal damage phenomenon observed in all mass-produced crystals is the appearance of absorption bands, caused by color-center formation. These absorption bands reduce the transmission of scintillation light in the crystals and hence the apparent light yield following irradiation. Additional effects observed in some crystals include reduced intrinsic yield of scintillation light, increased fluorescence (afterglow), and phosphorescence (spontaneous light emission over a long period). For a crystal to be used in a high-radiation environment, such as at multi-TeV hadron colliders, its scintillation mechanism must not be damaged and the radiation-induced phosphorescence must not affect the readout signal. Crystals such as $BaF_2$ or $CeF_3$ meet these criteria. However, the increased radiation-induced absorption (equivalently, a reduced light attenuation length) changes the light-response uniformity and thus may degrade the energy resolution.

### 5.1 *Radiation-Damage Phenomena*

The radiation-induced formation of color-centers and the decreased absorption length are usually related to impurities and/or structural defects in the crystals. The impurities may be present as substitutional or interstitial trace element atoms in the lattice, or they may occur as molecular ions or as microscopic color-center complexes containing many atoms. The extensive literature on high-purity silicon crystals and the specific studies of $BaF_2$ scintillators for the GEM Collaboration have shown that the impurities may also lead to macroscopic structures that are clusters of high-density, trace element–rich color centers. These structures form inclusions that are visible under a low power microscopic and, in some cases, to the naked eye.

Studies of the content and distribution of trace elements in the crystals, the quality of the crystal structure, and the density and structure

[2] See papers by Y. Dafinei, D. Hitlin, H. Newman, B. Winstein, C. L. Woody, and R. Y. Zhu (49).

of the inclusions in a series of crystal samples were conducted for BGO in 1981–1985 (26–28), and for $BaF_2$ from 1988–1993 (14, 21, 22). These data were cross-correlated with the degree of radiation damage in a series of doped and undoped crystal samples, which led to greatly improved processing technology for both types of crystals. As a result of the improved control of raw materials, crystal growth, and annealing methods, crystals with greater radiation resistance were produced, especially $BaF_2$. Studies of radiation damage for pure and doped CsI (17, 19), $CeF_3$ (18, 25), and $PbWO_4$ (32) are also underway.

Studies of BGO indicate that key impurities at levels of less than $10^{-6}$ may cause severe damage (27, 51). Figure 13 (27) shows the relative light output as a function of time after irradiation with a 2.5-krad dose for BGO samples doped with different dopants. These data led to the conclusion that impurities in the BGO crystal can be divided into three classes: *(a)* harmful impurities, which cause permanent or severe damage (Cr, Mn, Fe, and Pb); *(b)* less harmful impurities, which cause some damage (Co, Ga, Mg, and Ni); and *(c)* harmless impurities, which cause no discernible damage (Al, Ca, Cu, and Si) at the typical trace impurity levels found in standard-quality crystals. The figure also illus-

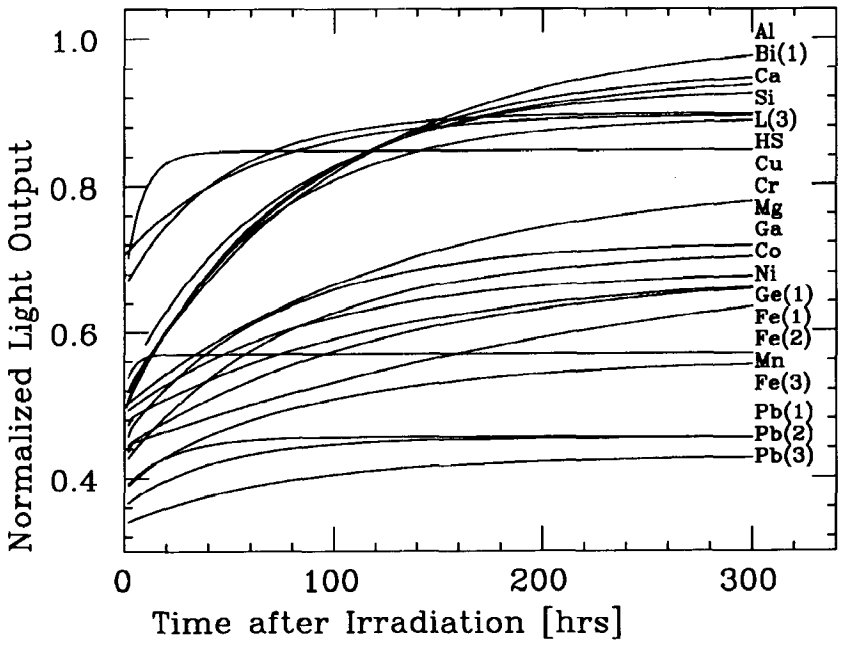


*Figure 13* Relative pulse height as a function of the time after irradiation with a 2.5-krad dose for BGO crystals doped with different dopants (27).

trates that various doped and undoped BGO crystal samples recover at different rates, with characteristic recovery times ranging from hours to weeks.

For BGO crystals, europium doping was found to improve radiation resistance by accelerating the recovery from damage that occurred at room temperature. Figure 14 (28) shows the relative pulse height as a function of time after a radiation dose of 2.5 krad from a $^{137}Cs$ $\gamma$-ray source for four BGO crystals doped with different amounts of europium: 0, 5, 10, and 100 ppm by weight for the samples labeled BGO0,

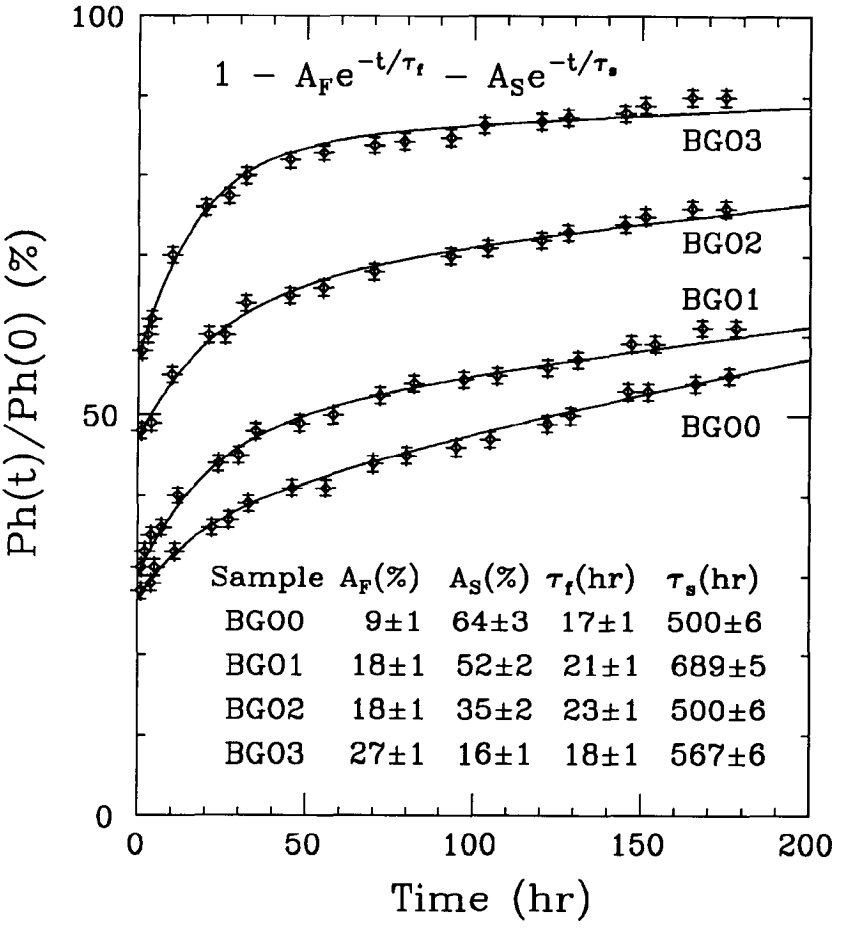


*Figure 14* Relative pulse height as a function of the time after a 2.5-krad $\gamma$-ray dose for 4 BGO crystals doped with different levels of europium: 0, 5, 10, and 100 ppm by weight for BGO0, BGO1, BGO2, and BGO3, respectively (28).

BGO1, BGO2, and BGO3, respectively, in the figure. The damage level is shown in terms of the parameters $A_F$ and $A_S$ from a fit to a function of $1 - A_F e^{-t/\tau_f} - A_S e^{-t/\tau_s}$. Clearly, the damage level ($A_F + A_S$), especially the slow-recovery component, decreases with increased europium doping. The europium-doped BGO crystals are used in the L3 BGO endcaps in rings closest to the beam line, where the dose is higher than in the barrel.

The main conclusions drawn from the investigations of radiation damage in $BaF_2$ crystals are as follows:

1. As in BGO, the damage in $BaF_2$ is caused by the formation of color centers, which introduce self absorption of the scintillation light. The scintillation mechanism itself remains unchanged.
2. Doses from photons, neutrons, or other hadrons (such as protons, pions, or kaons) cause no permanent damage in $BaF_2$. At room temperature, the recovery of the damage is extremely slow (characteristic times of many months to years). However, all damage recovers fully after thermal annealing at 500°C in an inert dry atmosphere for 3 h. UV light is also effective in removing the radiation damage.
3. The radiation damage in $BaF_2$ shows clear saturation, in both transmittance and light yield measured by the photosensor, after an initial dose of 100 krad or less. This means that higher doses result in no further change in transmittance once saturation has been reached. The saturation phenomenon indicates that the number of color centers is relatively few, as expected for damage centered on trace impurities.
4. The damage does not depend on the rate of irradiation.
5. The basic radiation damage mechanism is understood. Impurities (such as rare earths) (50, 52), defects (inclusions) (50, 53), oxygen (53), and $OH^-$ (U and $O^-$ substitutional centers) (54, 55) are responsible.

Figure 15 (14) shows *(a)* the transmittance before and after 1-Mrad $\gamma$-ray irradiation and *(b)* the relative light output measured for three 25-cm long $BaF_2$ crystals produced at the Shanghai Institute of Ceramics (SIC) in early 1991 (SIC102), early 1992 (SIC302), and July 1992 (SIC402). The progressive improvement of the production quality $BaF_2$ crystals is evident.

## 5.2 *Optical Bleaching in Situ*

The improvement of the intrinsic radiation resistance, by purification of the raw materials and the use of optimized growth and annealing

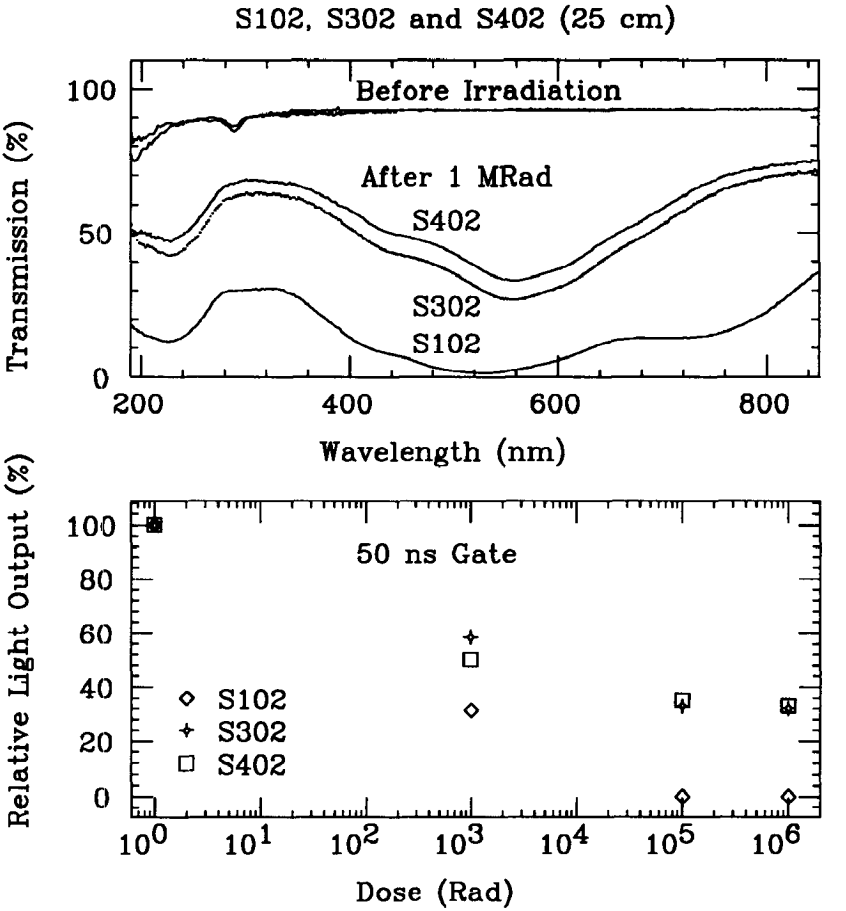


*Figure 15* *(a)* Transmittance and *(b)* relative light output measured for three 25-cm $BaF_2$ crystals produced at SIC in early 1991 (SIC102), early 1992 (SIC302), and July 1992 (SIC402), after a 1-Mrad $\gamma$-ray dose (14).

cycles, is a difficult, time-consuming, and expensive process. As evident from Figure 15, the light-attenuation length in 25-cm $BaF_2$ crystals produced at SIC and Beijing Glass Research Institute (BGRI) after 1 Mrad of saturated irradiation is rather short (42 cm) (46) and does not meet the GEM specifications (95-cm attenuation length) as of August 1992. A technique for annealing $BaF_2$ crystals in situ, i.e. optical bleaching, was proposed by a $BaF_2$ expert panel specially organized by the SSC Laboratory to evaluate the radiation damage problem of $BaF_2$ and assist in setting research directions for the development of $BaF_2$ crystals to be used at multi-TeV hadron colliders (57). Following the panel's

recommendations, five independent measurements on optical bleaching were carried out at BNL (58), Caltech (23), LLNL (59), Tsinghua and McGill Universities (60), and West Virginia University (61).

These experiments showed that optical bleaching with visible light effectively removed the radiation damage. Studies were also performed to characterize the spectral behavior, required light intensity, and rate of bleaching. The damage effect was found to be annealable with very low light intensities carried over silica fibers (58) and at wavelengths as long as 700 nm (23). The light intensity required to restore the crystals to a stable light attenuation length of at least 150 cm—well beyond the GEM specifications—was determined (23) to be in the range of a few $mW/cm^2$.

Figure 16 shows a practical implementation of optical bleaching through a 2-m-long 0.6-mm fiber. The crystal was simultaneously irradiated with a dose of 130 rads/h, and illuminated through the fiber with a calibrated light of 1.6 mW (integrated from 200–500 nm) from a 150-W xenon lamp. This modest amount of light resulted in a stable attenuation length of 170 cm (14), well in excess of the required value of 95 cm. The large opening angle of the light cone from the fiber (60°), and the reflection of the bleaching light at the crystal surface, ensure that the entire crystal is uniformly illuminated. For a large crystal calorimeter, the fiber system could be very similar to the xenon flasher system used to monitor the L3 BGO crystals described in Section 7.3.

Furthermore, the color-center density in $BaF_2$ crystals follows a simple dynamic model of color-center creation and annihilation (23). If both the creation and annihilation processes exist at the same time for one kind of color center, the density obeys the equation

$$dD = -aIDdt + (D_{all} - D)bRdt, \qquad 5.$$

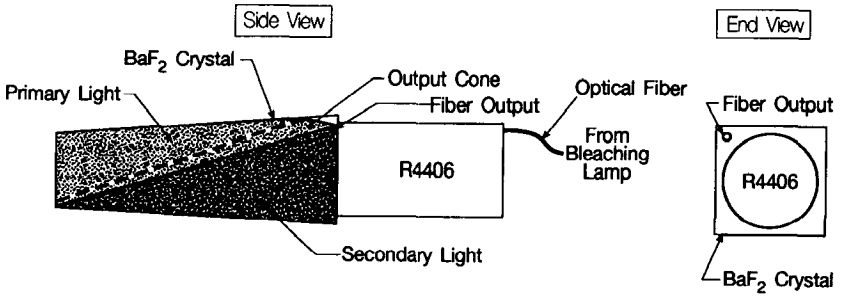


*Figure 16* Schematic view of bleaching light propagation in a $BaF_2$ crystal in the test setup used at Caltech, where light directly from fiber (primary light) has an open angle of 60°, while the reflected light (secondary light) covers the whole volume of the crystal.

where $D$ is the density of optically bleachable color centers; $a$ is a constant in units of $cm^2\ mW^{-1}\ hr^{-1}$; $I$ is the light intensity in $mW\ cm^{-2}$; $D_{all}$ is the total density of traps related to the optically bleachable color centers in the crystal; $b$ is a constant in units of $krad^{-1}$; $R$ is the radiation dose rate in units of krad $hr^{-1}$; and $t$ is the time in hours. The solution of Equation 5 is

$$D = D_0 e^{-(aI+bR)t} + \frac{bRD_{all}}{aI + bR}[1 - e^{-(aI+bR)t}], \quad 6.$$

where $D_0$ is the initial value of the bleachable color-center density. For each value of $I$ and of $R$ and for a given kind of color center, an equilibrium between annihilation and creation will be established at an optical bleachable color center density ($D_w$) of

$$D_w = \frac{bRD_{all}}{aI + bR}. \quad 7.$$

Figure 17 (14) shows the measured transmittance and the corresponding light-attenuation length for a series of test runs. The light-attenuation length corresponding to $D$ in Equation 6, calculated for the specific conditions of each run, is shown as the solid line. The parameters $a$, $b$, and $D_{all}$ were determined from previous measurements to be $a$ = 0.68 and 0.95 $cm^2/J$ for $D < 0.08$ and $D > 0.08$, respectively; $b$ = 0.65 $krad^{-1}$ for accumulated dose <5 krad, and $D_{all} = 0.73\ m^{-1}$. The agreement between the data and the model is very good.

## 5.3 *Summary*

In conclusion, a crystal to be used for constructing a precision calorimeter must maintain a long and stable light-attenuation length under irradiation, particularly in the high-radiation environment of multi-TeV hadron colliders. One approach to improve the intrinsic radiation resistance is to reduce the impurities and defects in the crystal. This modification, however, usually results in a very expensive crystal-fabrication. It is therefore important to understand the correlation between damage and impurities in the crystals and between damage and the details of the crystal-growth process. A high-quality crystal can only be produced with sufficiently pure raw material, appropriate preparation and handling of the material, and a corresponding carefully controlled growth technique. This is a cross-disciplinary research project, often requiring collaboration between physicists and materials scientists.

An alternative approach is to eliminate the radiation damage by means of either thermal or optical annealing. Recent studies on optical

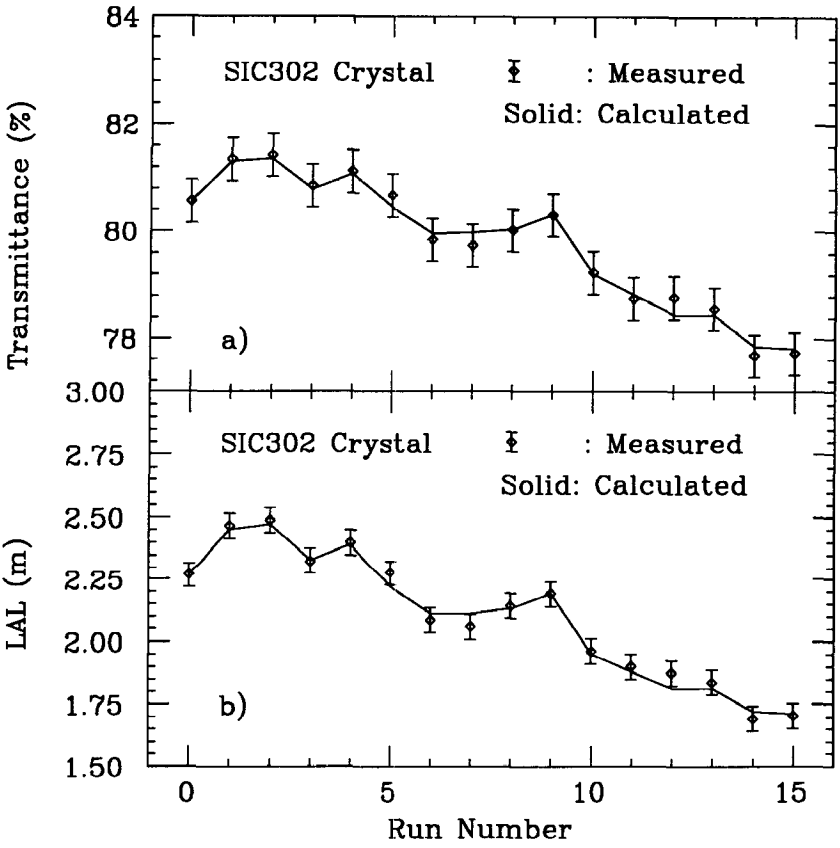


*Figure 17* Measured *(points)* and calculated *(solid line)* *(a)* transmittance and *(b)* light attenuation length (LAL) for the crystal SIC302 during a series of tests with simultaneous $^{60}$Co irradiation and 450-nm light illumination (14).

bleaching (23) show that optical bleaching is a practical solution for a $BaF_2$ calorimeter that would function stably, and with high resolution, at a multi-TeV hadron collider. The experience with $BaF_2$ suggests that once crystals of sufficient quality are produced, the optical bleaching technique could be applied to some other types of crystals as well.

## 6. READOUT ELECTRONICS

As discussed in Section 3, the front-end readout—the type and gain of photosensors and preamplifiers—is directly related to the performance of a crystal calorimeter. The choice of photosensor is affected by the

following factors: the magnetic field surrounding the detector, the scintillation light yield and wavelength of the crystal, and the energy-equivalent noise per readout channel. Tables 2 and 3 list some of the principal performance-related parameters of the photosensors for various crystal calorimeters.

The traditional photosensor is the vacuum photomultiplier tube (PMT) (Crystal Ball, CUSB, and KTeV), which has the advantages of high gain, low noise, low capacitance, and high radiation resistance up to neutron fluences of $10^{14}$ cm$^{-2}$ s$^{-1}$ (62). The spectral response of different photocathodes is also a useful feature for a vacuum photosensor. For example, solar-blind photocathodes (37) have been used to select the fast scintillation components of $BaF_2$, as shown in Figure 11.

Because of these factors, some crystal calorimeters designed for multi-TeV hadron colliders use vacuum photosensors. For example, a design simulation for the $BaF_2$ calorimeter (46) has shown that with a low-gain vacuum photosensor of 20 pF capacitance, a charge-equivalent noise of ~1000 electrons (including the effect of pileup from additional tracks in the same event) could be achieved with a shaping time approaching 1 bunch-crossing time. This corresponds to an energy-equivalent noise of ~3 MeV/channel.

Because a magnetic field is present on the photosensors, most calorimeters now in operation or recently designed (CLEO II, L3, Crystal Barrel, and B factories) use large-area (a few cm$^2$ and a few hundred pF capacitance) silicon photodiodes (Si PD). Because of the low gain of these photosensors, a preamplifier with sufficiently low noise, high gain, and good linearity over a large dynamic range is required. Except for high-rate hadron colliders, the decay-time constant of the preamplifier pulse is chosen in the millisecond range, and the pulse is shaped by a pole-zero circuit connected to the ADC. To minimize noise, the typical shaping time (in these lower-rate applications) is a few $\mu$s. Figure 18 (5) shows as an example the CLEO II front-end electronics. Each crystal is read out by four photodiodes and four preamplifiers to provide redundancy. Analog signals from clusters of contiguous crystals are summed with individually adjustable gain factors and are fed to the first level of energy trigger.

Recently, we have seen some important developments in photosensors. Proximity focused, few-stage, grid mesh tubes developed by Hammamatsu (38) function in a magnetic field up to 1 Tesla, though at relatively high cost. A similar approach is to use a microchannel plate (MCP), which also has appropriate gain, speed, and—in some cases—relative immunity to magnetic fields. The principal drawbacks

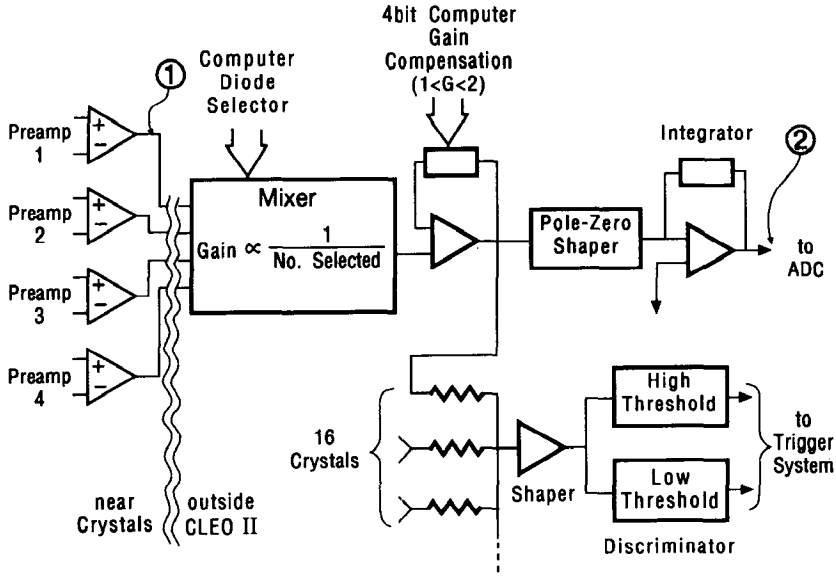


*Figure 18* Block diagram of the CLEO II front-end electronics and signal shaping (5). For reasons of redundancy, individual preamplifiers have been used for each of the four photodiodes attached to a single crystal. The mixing of the four signals and the suppression of malfunctioning readout circuits is performed by a computer-controlled mixer stage.

of MCPs are their high cost and relatively fast aging. On the other hand, both the solid-state equivalent of PMTs (63), and large-area avalanche photodiodes (APDs) (64), have been refined so that their noise, stability, and gain values make them highly competitive as photosensors, especially for lower energy measurements. However, the intrinsic temperature dependence ($-2\%/°C$) of the gain must be taken into consideration when APDs are chosen as the photosensor.

As shown in Tables 2 and 3, a dynamic range near $10^5$ is not uncommon, even though it is extremely difficult to achieve. Indeed, most crystal calorimeters built to date show small nonlinearities of a few percent over their energy range, which adds to the difficulty of overall detector calibration. A logarithmic amplifier could reduce the dynamic range and simplify the design of the read-out circuit. However, the accuracy of such amplifiers and their low speed make them unsuitable for most applications. Most designs therefore include a split of the signal in the electronic readout for each channel, followed by several parallel branches with different gains and hence different (overlapping)

energy ranges. Note that the large dynamic range requirement can be met with ADCs of sufficient speed and linearity. The issue in a large system with many thousands of channels thus becomes one of cost, or of careful design and future developments and study.

## 7. CALIBRATION TECHNIQUES

Once crystals of sufficient length, light output, uniformity of response, speed, and radiation resistance are chosen to meet the needs of a particular experiment, the precision of the calibration performed in situ is the dominant factor in determining the resolution for electron and photon measurements during operation. Although all the individual cells of a crystal calorimeter may be calibrated in a test beam at several different energies to provide a set of initial calibration constants before installation (4), the change in response over time differs from one calorimeter element (crystal, photodetector, readout chain) to the next. Calibrations in situ are therefore required to track the evolution of each channel independently. The time evolution may depend strongly on the position in the calorimeter, and the radiation damage could locally degrade the light uniformity and thus the resolution. Figure 19 (65) shows the radiation-induced change in the response, and the longitudinal response profile, of an L3 BGO crystal situated near the LEP beam line. The effect of the damage is more severe in the front section of the crystal.

The task of calibration can be divided into two steps: *(a)* finding the absolute energy scale of the calorimeter (absolute calibration) and *(b)* measuring the channel-to-channel relative gains (intercalibration). The accuracies of these two procedures affect the mean value of the measured energy as well as the resolution. In many cases, every method of calibration available to the experimenters (and additional methods developed for this purpose in the case of L3) is used to obtain and maintain a sufficiently precise calibration in situ. Figure 20 shows the energy range and the corresponding time required to complete a calibration for the various calibration techniques used for the L3 BGO calorimeter. No single technique can, by itself, guarantee calibration of better than 1% of the many thousands of channels over many months and over the full energy range. A variety of different techniques must be combined to provide a high level of understanding and control of systematics.

In this section, we discuss in situ calibrations using high-energy physics processes, low-energy $\gamma$ rays produced by radioactive sources and radiative capture nuclear reactions, and light flashers.

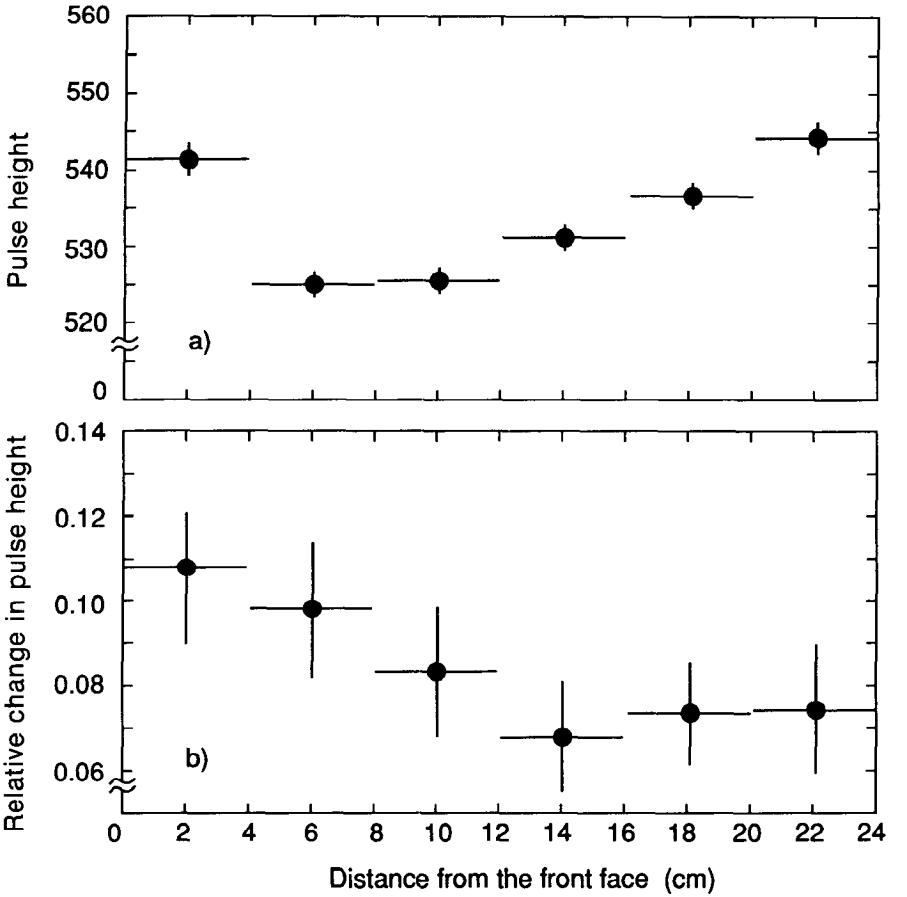


*Figure 19* *(a)* Effect of radiation exposure as a function of the longitudinal distance from the front end for L3 BGO crystals at LEP: crystal response to a constant energy deposition by minimum ionizing particles. *(b)* The normalized difference of response for data recorded five months apart (65).

## 7.1 *Physics Processes*

Using physics processes is the most common method for in situ calibration because it covers the appropriate energy range and does not require additional hardware. Methods based on physics processes include electrons or photons of known energy, electron or photon pairs that can be used to reconstruct the invariant mass of a known particle, low-energy electrons with momentum accurately measured by a magnetic spectrometer, and minimum ionizing particles that penetrate a crystal with measured path length.

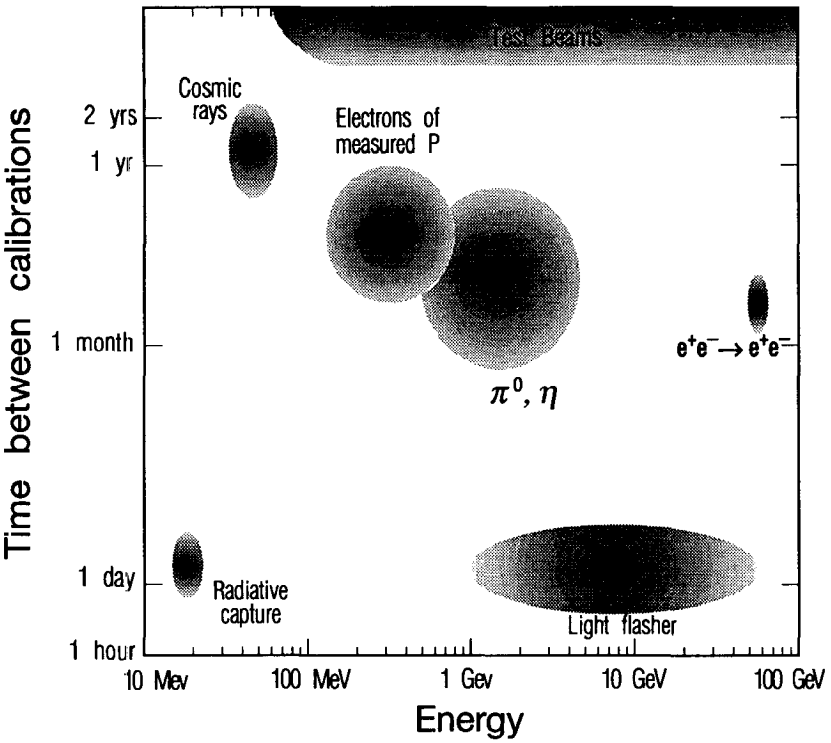


*Figure 20* Energy range and frequency of calibration techniques applied in the L3 experiment.

At $e^+e^-$ colliders, Bhabha scattering ($e^+e^-$ elastic scattering) produces electrons of energy close to that of the beam. The beam energy is widely used as a high-energy calibration point. Some care must be taken to understand and unfold the effects of initial- and final-state photon radiation (bremsstrahlung) that broaden the electron energy distribution and produce a tail on the low-energy side. Crystal Ball has been able to find high-energy corrections to their low-energy calibration on a channel-by-channel basis by using Bhabha events (1, 41). The rate of such events in L3, on the Z peak, is too low at the present LEP luminosity (~6 electrons/crystal per year on average for the barrel) to be used as the basis of an intercalibration. However, enough of these events occur in L3 to establish the high-energy scale with negligible statistical error once crystal-to-crystal differences and time drifts have been corrected independently.

Photons from radiative dilepton events also can be used as a calibra-

tion source through the precise measurement of the leptons and the use of the beam energy constraint in $e^+e^-$ collisions. For example, CLEO II's absolute calibration is set by photons from the processes $e^+e^- \rightarrow e^+e^-(\gamma)$, $e^+e^- \rightarrow \gamma\gamma$, $e^+e^- \rightarrow \gamma\gamma\gamma$, and $e^+e^- \rightarrow \pi^0 X$, although the whole calorimeter can be intercalibrated with Bhabha events alone in approximately one week (5). These photons provide CLEO II with the best energy calibration over the entire range from a few MeV to 5 GeV. The need for calibration as a function of energy is demonstrated by the fact that CLEO II observes an energy-dependent shift between electrons and photons, as illustrated in Figure 21 (5).

Invariant mass reconstruction using photon or electron pairs from a boson with known mass is also a powerful calibration tool. In general, only the global energy scale is determined by this method. In the Crystal Barrel experiment, however, the rate of $\pi^0$ production is large enough to calibrate each crystal of the calorimeter in approximately one day

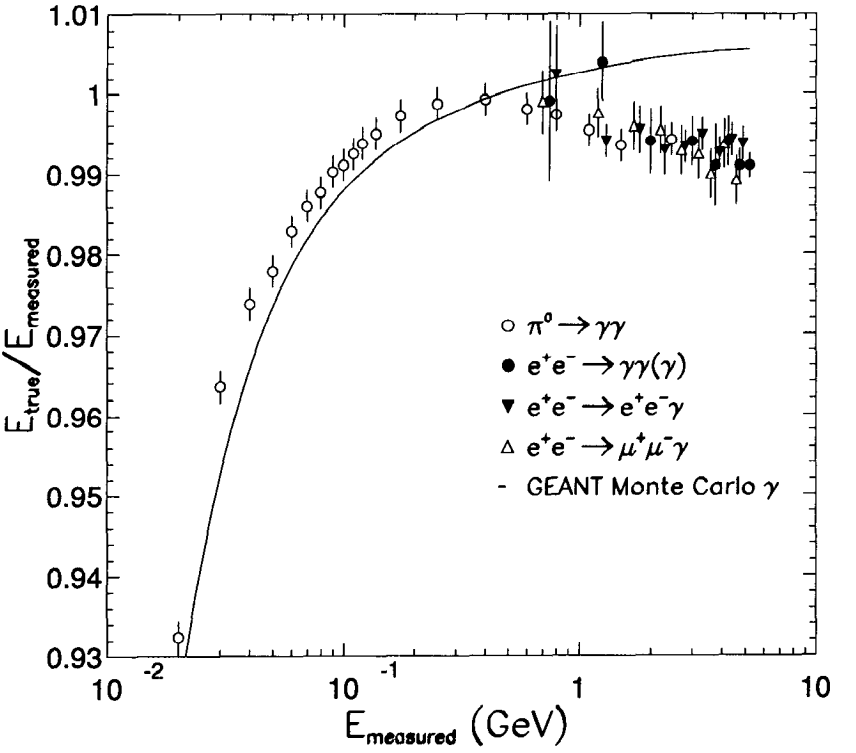


*Figure 21* The correction factor ($E_{true}/E_{measured}$) for absolute photon energy calibration, measured using different physics processes in CLEO II as a function of the photon energy (5).

with a statistical error of $\pm 0.5\%$ (6). Studies of crystal calorimeter calibration at the SSC show that an accuracy of 0.3% can be achieved after less than one month of running at a luminosity of $10^{33}$ cm$^{-2}$ s$^{-1}$ by reconstructing the $Z$ mass in $Z \rightarrow e^+e^-$ decays (14). This iterative procedure needs a set of initial calibration constants accurate to ~20%, which could be provided by measuring the energy deposition of minimum ionizing particles crossing the crystals longitudinally.

In most of the modern collider detectors, a momentum measurement is available for charged particles before they enter the electromagnetic calorimeter. The reconstructed momentum for isolated electrons, where the corresponding electromagnetic shower is well separated from the energy deposited by other particles, therefore provides an alternate energy reference that may be used for calibration. Because the momentum measurement degrades with increasing energy while the calorimetric energy measurement improves, this technique is generally useful only for relatively low-energy particles. Very often in practice (as on the $Z^0$ resonance at an $e^+e^-$ collider), the isolation requirement and the restriction to low-momentum tracks limit the effective rate of useful events, so that this technique may serve only as a check for the calorimeter resolution.

Both cosmic rays and a substantial fraction of the charged particles emerging from high-energy interactions may be used as a source of minimum ionizing tracks. For detectors with pointing geometry, final-state particles might traverse one crystal longitudinally, whereas a cosmic-ray track generally leaves energy in many crystals. To use these tracks to perform a calibration, the path length of the track traversing the crystal must be known precisely so that the deposited energy in a crystal can be calculated with sufficient accuracy.

L3 uses its large precise muon spectrometer to measure the path length of cosmic rays penetrating a crystal. However, the multiple scattering in the ~7 interaction length hadron calorimeter between the muon spectrometer and the electromagnetic calorimeter reduces the tracking precision. Only muons above 10 GeV momentum and which diametrically cross the crystal array are used. For these tracks, the path length inside the crystal depends only slowly on the impact point. The energy distribution observed has a shape dominated by Landau fluctuations (65), with an rms width of 18%, and the energy deposited is typically 20 MeV. L3 can collect only 130,000 useful cosmic rays per day so that several months of dedicated data taking are needed to determine the peak position for every crystal with a precision of 1%. However, this technique is not practical because the calorimeter response in each channel may change significantly during this long period.

Studies of monitoring the gain of individual crystal using charged particles from high-energy interactions at multi-TeV hadron colliders show that a precision of 0.3% could be achieved in a few hours, using a dedicated trigger at a rate of >1 kHz at a luminosity of $10^{33}$ $cm^{-2}$ $s^{-1}$ (40). A higher-rate dedicated trigger also could be implemented (at higher cost).

## 7.2 *Radioactive Sources and Radiative Capture Reactions*

Low-energy $\gamma$ rays from radioactive sources or from radiative capture reactions are often used as a low-energy calibration source. Their use is particularly important in crystal calorimeters for which physics processes do not occur at a high enough rate for a frequent calibration, e.g. the L3 BGO calorimeter. Radioactive sources are relatively inexpensive and have very small dimensions, so they can be directly mounted on each crystal to monitor the calorimeter continually during its lifetime. Using this technique, CUSB has been able to intercalibrate its detector, with the absolute energy fixed by using 5-GeV electrons (from $e^+e^- \rightarrow e^+e^-$) and by photons from $\pi^0$ decays (3). The disadvantages of the use of radioactive sources are the limited energy range and the necessity of triggering on a signal that is random in time.

The maximum energy photon easily available from a long-lived radioactive source is the 2.6-MeV line of $^{228}$Th. The 0.66-MeV line of $^{137}$Cs and the 1.17- and 1.33-MeV lines of $^{60}$Co (which are typically measured as one peak in large crystals) are more commonly used (3, 66). In many cases, including all calorimeters using silicon photodiode readouts, the signals from radioactive sources are very small, too close to the pedestal, or even overlapping with the noise, so that they are not useful as a means of calibration.

Photons with energies an order of magnitude higher can be produced using radiative-capture reactions by bombarding a target mounted inside the calorimeter with a proton beam of suitable energy. This technique was pioneered by Crystal Ball (66) with the use of a Van de Graaf accelerator to produce the proton beam. The same technique is now used by L3 in a more sophisticated implementation, with a radiofrequency quadrupole (RFQ)–based accelerator system (67), as shown in Figure 22.

Whereas Crystal Ball used a set of reactions that produced photons from 2.2–17.6 MeV, L3 concentrated on the 17.6-MeV line from the reaction

$$p + {}^{7}_{3}\mathrm{Li} \rightarrow {}^{8}_{4}\mathrm{Be} + \gamma. \qquad 8.$$

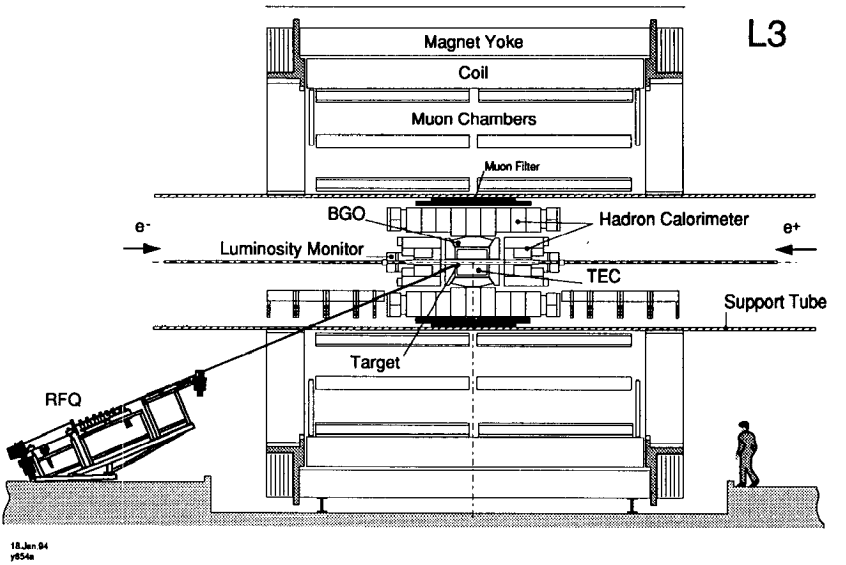


*Figure 22* Layout of the RFQ calibration system for the L3 BGO calorimeter.

This is the highest energy attainable with nonrefrigerated targets (the reaction $p + {}^{3}_{1}\mathrm{H} \rightarrow {}^{4}_{2}\mathrm{He} + \gamma$ yields 21.6 MeV but requires a cryogenic tritium target). A synchronized trigger is provided by pulsing the proton beam. Because most of the 14-m beam transport line and the lithium target are in a 0.5-T magnetic field, a neutral hydrogen beam is produced by stripping an electron away from the $H^-$ ions outside of the magnetic volume, using a low-pressure ($5 \times 10^{-4}$ torr) nitrogen gas cell. RFQ calibration runs in 1993, with limited statistics, resulted in a resolution of 0.99% for 45-GeV electrons from Bhabha scattering events (after unfolding the radiative tail). With the higher beam intensity expected in 1994, the overall calibration precision is expected to improve. At the design intensity of the RFQ beam, 1% precision could be reached in a single calibration run of ~1 h.

An extension of this technique (68) uses the high cross section of the reaction

$$p + {}^{19}_{9}\mathrm{F} \rightarrow \alpha {}^{16}_{8}\mathrm{O}^{*} \rightarrow \gamma + {}^{16}_{8}\mathrm{O} \qquad 9.$$

to produce a large number of 6.1 MeV photons for each RFQ bunch (a few microseconds long). The photons pile up in the calorimeter readout gate, resulting in an effective energy of several GeV in each crystal. With this technique, which is particularly suitable for crystal calorime-

ters at multi-TeV hadron colliders, an accuracy of 0.4% has been achieved in a few minutes for the L3 BGO system (68).

## 7.3 *Light Pulsers*

A light-pulser system is a useful tool to monitor the light transmittance in crystals, the reflectivity of the crystal wrapping or coating, and the readout gain. As discussed in Section 5, the scintillation mechanism of most crystals is not damaged by irradiation. The light pulser thus can serve as another means of intercalibration.

Figure 23 illustrates the L3 xenon flasher system (69). A light pulse is generated by a high-intensity xenon flash lamp. The pulse is filtered to approximately reproduce the BGO scintillation spectrum. The light is then transported by a set of optical fibers to the individual crystals of the calorimeter and to various devices monitoring the intensity. Usually some diffuse medium is inserted in the optical path to ensure uniform light distribution among the fibers. Fibers are selected to be radiation resistant, and some of the intensity monitoring devices are located as close as practical to the calorimeter, so that possible fiber aging can be detected. In general, no attempt is made to provide a source of stable intensity; rather, the intensity is precisely measured on a pulse-to-pulse basis by photodiodes and phototubes maintained in a controlled environment.

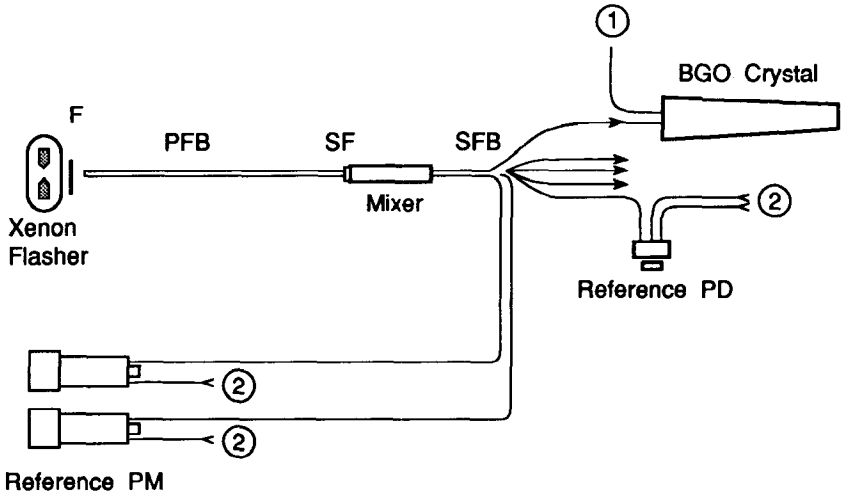


*Figure 23* Schematics of the L3 xenon light pulser system used in L3. PFB, primary fiber bundle; SFB, secondary fiber bundle; F, attenuation filter; SF, spectral filters. (1) Fiber from a second lamp. (2) Fibers from other mixers.

The light-pulser system is fast and easy to operate; hence it is very useful for tracking changes in the detector response over short periods of time. Because the relative amount of light carried by each fiber is not known a priori, a reference to an absolute calibration, e.g. a beam test, has to be established. Subsequent changes in the intercalibration (particularly those associated with overall light transmission through the crystals to the photosensor, and with the relative gain of each readout chain) can be tracked. A precise set of temperature sensors must also be employed because the scintillation light yield of BGO is a function of temperature (with a coefficient of $-1.6\%/°C$) and the light-pulser system does not check the scintillation efficiency of the crystals.

The L3 calorimeter was initially intercalibrated using a test beam. Since then it has been continuously monitored using a light-flasher system. By combining the results of the xenon light flasher with Bhabha events, a resolution of 1.22% at 45 GeV was obtained after ~3 years of L3 running.

## 8. CONCLUSION: PHYSICS WITH CRYSTAL CALORIMETERS

The high resolution and uniform and hermetic coverage of homogeneous crystal calorimeters has given past and present experiments unique potential for physics discovery. Over the past two decades, large calorimeters of this type have achieved resolutions that meet or approach their design values. The only limitations have been traced to the gain calibration, which fundamentally depends on the availability of sufficient physics calibration processes combined with quick precise monitoring methods, and to possible radiation damage.

The special physics capabilities of these detectors are clearly illustrated by the search for the Higgs boson—the key missing piece of the otherwise highly successful standard model of the fundamental interactions—in the mass range between 80 and 170 GeV in multi-TeV hadron colliders (43).

Figure 24 shows the $\gamma\gamma$ invariant mass spectra predicted for one year of operation at the SSC ($10^4$ pb$^{-1}$) for Higgs masses of 80, 100, 120, 140, and 160 GeV, superimposed on the irreducible-background. The mass spectra are shown for three energy resolutions: $(2/\sqrt{E} \oplus 0.5)\%$ (for a crystal calorimeter), $(7.5/\sqrt{E} \oplus 0.5)\%$ for a liquid-argon calorimeter), and $(15/\sqrt{E} \oplus 1.0)\%$ (for a sampling calorimeter). The irreducible background results from direct production of photon pairs not associated with the Higgs, i.e. predominantly from gluon-gluon scattering.

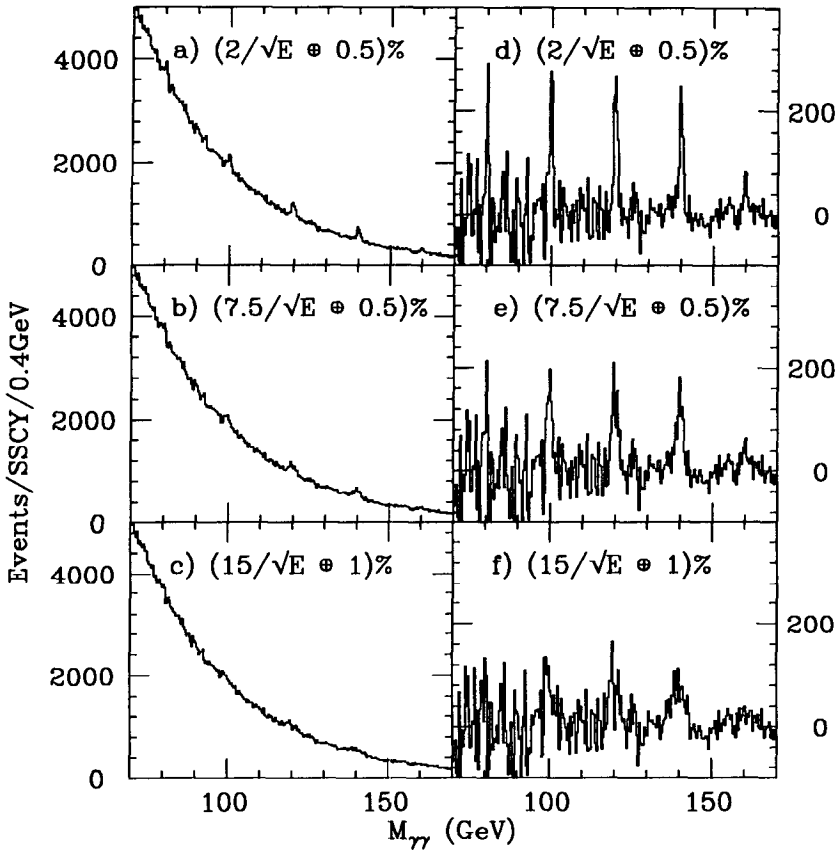


*Figure 24* Invariant $\gamma\gamma$ mass spectra predicted for the production of Higgs particles of 80, 100, 120, 140, and 160 GeV during one year of operation of the SSC (10 $fb^{-1}$ at 40 TeV). The spectra are shown *(a–c)* superimposed on irreducible background, and *(d–f)* after statistical subtraction of the background. The mass spectra are given for three resolutions corresponding to three calorimeter types: $(2/\sqrt{E} \oplus 0.5)\%$ ($BaF_2$), $(7.65/\sqrt{E} \oplus 0.5)\%$ (liquid argon), and $(15/\sqrt{E} \oplus 1.0)\%$ (sampling calorimeter).

Figure 25 shows the significance obtainable in a Higgs search as a function of the integrated luminosity, expressed in units of standard SSC years (SSCY), for Higgs masses of 80, 90, 100, 120, 140, 150, and 160 GeV. In this figure the significance is plotted as a band for each energy resolution. The upper edge of the band corresponds to the irreducible $\gamma\gamma$ background, while the lower edge of the band takes into account the background resulting from hadron jets misidentified as photons. The advantage of the high resolution of crystal calorimeters in

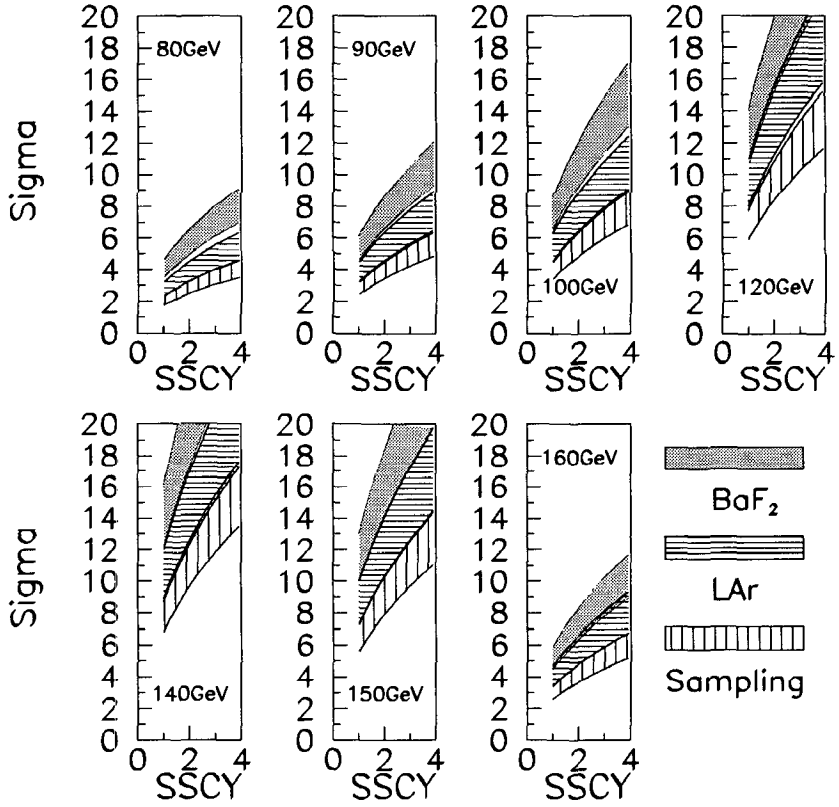


*Figure 25* The significance in units of standard deviations of the $H \rightarrow \gamma\gamma$ signal as a function of the integrated luminosity in units of $10^{40}$ cm$^{-2}$ (1 standard year at the SSC) for Higgs masses of 80, 90, 100, 120, 140, 150, and 160 GeV and for the following resolutions: $(2/\sqrt{E} \oplus 0.5)\%$ ($BaF_2$), $(7.5/\sqrt{E} \oplus 0.5)\%$ (LAr), and $(15/\sqrt{E} \oplus 1.0)\%$ (sampling).

searching for the Higgs in this difficult mass region is clearly demonstrated.

To reach and maintain this resolution, speed, radiation hardness, and precision intercalibration in situ are among the primary requirements for future multi-TeV hadron colliders. Recent extensive research and development has demonstrated that mass-produced crystals of sufficient quality could be obtained and stable uniform response and the intrinsic resolution achieved (through optical bleaching) to meet these requirements. The knowledge we have gained during the $BaF_2$ program (as discussed above) and from recent studies of other scintillating crystals by SIC, BGRI, Caltech, and member groups of the CMS and Crys-

tal Clear collaborations, leads us to believe that a precision crystal calorimeter could play a key role in the physics program of the next generation of hadron colliders. To achieve the requisite stability and uniformity of response for crystals that are denser and potentially more cost-effective than $BaF_2$ further research and development is required.

## ACKNOWLEDGMENTS

In the preparation of this report we benefited greatly from discussions with many physicists who have contributed to the development of precision crystal calorimeters or were among the innovators who have realized the discovery potential of these detectors. The work reported here would not have been possible without their contributions. We would like to express our sincere thanks to Drs. D Anderson, B Barrish, C Barnes, A Bay, E Bloom, B Borgia, J Branson, M Cavalli-Sforza, G Chen, M Chen, P Denes, M Doser, G Eigen, A Engler, M Fukushima, L Halliburton, B Heltsley, D Hitlin, H Hofer, Y Kamyshkov, R Kavanaghe, M Kobayashi, H Kobrak, K Königsmann, M LeBeau, P LeCoq, P J Li, E Longo, E Lorenz, D Marlow, S Majewski, T Matsuda, M Merk, F Nessi-Tedaldi, F Pauss, C Peck, P Piroue, F Porter, M Schneegans, P Schotanus, X Shi, K Shmakov, M Strathman, SCC Ting, T Tombrello, J Urheim, M Vivargent, T J Virdee, H Vogel, A Weinstein, Z Wei, B Winstein, C Woody, C Wuest, D S Yan, and Z W Yin. This work was supported in part by US Department of Energy Grant No. DE-FG03-92-ER40701 and Texas National Research Laboratory Commission Grants Nos. RGFY92-120 and RGFY93-313.



*Literature Cited*

1. Oreglia M, et al. *Phys. Rev.* D25:2295 (1982)
2. Bloom E, Peck C. *Annu. Rev. Nucl. Part. Sci.* 33:143 (1983)
3. Böringer T, et al. *Phys. Rev. Lett.* 44: 1111 (1980); Mageras G, et al. *Phys. Rev. Lett.* 46:1115 (1981)
4. L3 Collaboration. *Nucl. Instr. Methods* A289:35 (1990)
5. Kubota Y, et al. *Nucl. Instr. Methods* A320:66 (1992)
6. Aker E, et al. *Nucl. Instr. Methods* A321:69 (1992)
7. Arisaka K, et al. *KTeV Design Report.* FN-580, January (1992)
8. BaBar Status Report, SLAC-419, June (1993)
9. *1992 Progress Rep. B Phys. Task Force Act., KEK Rep.* 93-1, January (1993)
10. *L* Lett. Intent SSC Lab.*, November (1990)
11. *GEM Lett. Intent, SSCL SR-1184,* November (1991)
12. *Compact Muon Solenoid Lett. Intent, CERN/LHCC 92-3, LHCC/I1* (1992)
13. *L3P Lett. Intent, CERN/LHCC 92-5, LHCC/I3* (1992)
14. Zhu RY. *Nucl. Instr. Methods* A340: 442 (1994)

15. Harshaw QS. *Scintillation Detectors*. March (1992)
16. BDH Limited. BDH Crystran—Monocrystal Products for Optics, January (1990)
17. Wei ZY, Zhu RY. *Nucl. Instr. Methods* A326:508 (1993)
18. Crystal Clear Collaboration. *CERN-DRDC* 93-31 (1993); *Nucl. Instr. Methods* A332:373 (1993)
19. Kobayashi M, Sakuragi S. *Nucl. Instr. Methods* A254:275 (1987); Bieler C, et al. *Nucl. Instr. Methods* A234:435 (1985); Grassmann H, et al. *Nucl. Instr. Methods* A228:323 (1985); Schlogl S, et al. *Nucl. Instr. Methods* A242:89 (1985); Woody C, et al. *IEEE Trans.* NS-37:492 (1990); 39:524 (1992); Hitlin D, Eigen G. See Ref. 49, p. 467 (1992)
20. Schotanus P, et al. *Nucl. Instr. Methods* A238:564 (1985); Kobayashi M, et al. *Nucl. Instr. Methods* A270:106 (1988)
21. Majewski S, Anderson D. *Nucl. Instr. Methods* A241:76 (1985); Majewski S, Bently MK, *Nucl. Instr. Methods* A260:373 (1987)
22. Caffreay AJ, et al. *IEEE Trans.* NS-33: 230 (1986); Murashita M, et al. *Nucl. Instr. Methods* A243:67 (1986); Marakami A, et al. *Nucl. Instr. Methods* A253:163 (1986); A301:435 (1991); Woody CL, et al. *IEEE Trans.* NS-36: 536 (1989); NS-39 123 (1992); Wei ZY, et al. *Nucl. Instr. Methods* B61:61 (1991)
23. Ma DA, Zhu RY. *Nucl. Instr. Methods* A332:113 (1993)
24. Anderson DF. *IEEE Trans.* NS-36:137 (1989); Moses WW, Derenzo SE. *IEEE Trans.* NS-36:173 (1989)
25. Woody CL, et al. *BNL-49866, IEEE Trans. Nucl. Sci.* (1994). Submitted
26. Kobayashi M, et al. *Nucl. Instr. Methods* A206:107 (1983); Laviron C, Lecoq P. *Nucl Instr. Methods* A227:45 (1984); Bobbink GJ, et al. *Nucl Instr. Methods* A227:470 (1984); Bieler C, et al. *Nucl. Instr. Methods* A234:435 (1985)
27. Zhu RY, et al. *Nucl. Instr. Methods* A302:69 (1991)
28. Wei ZY, et al. *Nucl. Instr. Methods* A297:163 (1990)
29. Kobayashi M, et al. *Nucl. Instr. Methods* A335:509 (1993)
30. Dally EB, Hofstadter R. *Rev. Sci. Instr.* 39:658 (1968); Anderson DE, et al. *Nucl. Instr. Methods* A290:385 (1990); Woody CL, et al. *IEEE Trans.* NS-40:546 (1993)
31. Melcher CL, Schweitzer JS. *Nucl. Instr. Methods* A314:212 (1992); *IEEE Trans.* NS-39:502 (1992)
32. Crystal Clear Collaboration. *CERN-DRDC* 93-31 (1993); Woody CL, et al. *Phenix Note PX-63* (1993)
33. Anderson DF, et al. *Nucl. Instr. Methods* A342:473 (1994); Wuest CR, et al. Presented at Crystal Clear Collaboration Meeting, *CERN*, December (1993)
34. Kobayashi M, et al. *Nucl. Instr. Methods* A333:429 (1993)
35. Suzuki H, PhD thesis. Calif. Inst. Technol., Pasadena, CA (1994)
36. Worden HM. PhD thesis. Cornell Univ., Ithaca, NY (1992)
37. Hamamatsu Photonics K.K. *R4406 specification* (1990)
38. Suzuki S. *Proposal to Develop a Remote Processed Proximity Focused Phototube*. July (1992)
39. Brun R, et al. *GEANT3, CERN DD/EE/84-1* (1987)
40. Shmakov K. *GEM TN-92-143*, August (1992)
41. Oreglia M. PhD thesis, Stanford Univ., Stanford, CA *SLAC Rep. 236* (1980)
42. Kobayashi M, et al. *Nucl. Instr. Methods* A305:401 (1991)
43. Zhu RY, Yamammoto H. *GEM TN-92-126; CALT 68-1802* (1992)
44. Merk M. *Study of Bhabha scattering at $Z^0$ resonance using the L3 detector*. PhD thesis. Nijmegen Univ., Holland (1992)
45. Clayton E, et al. *CMS TN/92-50; IC HEP/93-1* (1992)
46. Denes P. *GEM TN-91-06* (1991)
47. Schotanus P, et al. *IEEE Trans.* NS-34:272 (1987); *Nucl. Instr. Methods* A281:162 (1989); Woody CL, et al. *IEEE Trans.* NS-36:536 (1989)
48. Deleted in proof
49. Nataristefani F, et al, eds. *Proc. "Crystal 2000" Int. Workshop*, Charmonix France, Sept. 22–26, 1992, Vol. C58. Gif-sur-Yvette: Editions Frontieres (1992)
50. Strathman M. Material Characterization of $BaF_2$ Samples. June–August (1992)
51. Zhou TQ, et al. *Nucl. Instr. Methods* A258:58 (1987)
52. Chen G, et al. In *Supercollider 4*, ed. J. Nonte, p. 809. New York: Plenum (1992)
53. Li PJ, et al. In Supercollider 4, ed. J Nonte, p. 801. New York: Plenum (1992); Yin ZW. Presented at East Asia/Pacific-US Symposium on SSC (1992)

54. Chen LY, et al. *GEM TN-92-129* (1992); Wang L, et al. Presented at Shanghai $BaF_2$ Workshop, Shanghai. (1991)
55. Halliburton LE, et al. *Univ. W. V. Optoelectron. Group Tech. Rep.* April–August (1992)
56. Ma DA, Zhu RY. *Nucl. Instr. Methods* A333:422 (1993)
57. Majewski S, et al. *$BaF_2$ Expert Panel Rep.* February and August (1992)
58. Stoll SP. *BNL Rep.* August (1992)
59. Wuest CR, Mauger GJ. *LLNL Rep.* August (1992)
60. Shang RC. *Optical Annealing of $BaF_2$ Crystals with Laser Beam,* August (1992)
61. Halliburton LE, et al. *Univ. West Virginia Optoelectron. Group Tech. Rep.* April–August (1992)
62. Moszynski M, et al. *Nucl. Instr. Methods* A226:534 (1984)
63. Allam J, et al. *IEEE Trans.* EDL-8:4 (1987); Capasso F, et al. *Appl. Phys. Lett.* 48:1294 (1986); *IEEE Trans.* EL-30:381 (1983); Petroff M, et al. *Appl. Phys. Lett.* 51:406 (1987)
64. Capasso F. In *Semiconductors and Semimetals,* ed. RK Willardson, AC Beer 22:2. New York: Academic (1985); Eigen G, Hitlin D. See Ref. 49, p. 539 (1992)
65. Bakken J, et al. *CERN-PPE/93-184* (1994) Submitted to *Nucl. Instr. Methods*
66. Chan Y, et al. *IEEE Trans.* NS-25:333 (1978)
67. Ma H, et al. *Nucl. Instr. Methods* A274:113 (1989); Gratta G, et al. *L3 Internal Note* 1557 (1993)
68. Ma H, et al. *Nucl. Instr. Methods* A281:469 (1989); Zhu RY. *Nucl. Instr. Methods* A306:145 (1991)
69. Bay A, et al. *Nucl. Instr. Methods* A321:119 (1992)

*Annual Review of Nuclear and Particle Science*
*Volume 44, 1994*

# CONTENTS